Atmospheric Research 187 (2017) 42–56

Contents lists available at ScienceDirect

Atmospheric Research

journal homepage: www.elsevier.com/locate/atmosres

Model analysis of soil dust impacts on the boundary layer meteorology and air quality over East Asia in April 2015

Lei Chen [a,b], Meigen Zhang [a,c,*], Jia Zhu [a,b], Andrei Skorokhod [d]

[a] State Key Laboratory of Atmospheric Boundary Layer Physics and Atmospheric Chemistry (LAPC), Institute of Atmospheric Physics (IAP), Chinese Academy of Sciences (CAS), Beijing 100029, China
[b] University of Chinese Academy of Sciences, Beijing 100049, China
[c] Center for Excellence in Urban Atmospheric Environment, Institute of Urban Environment, Chinese Academy of Sciences, Xiamen, China
[d] Laboratory of Atmospheric Gas Species, A.M. Obukhov Institute of Atmospheric Physics, Russian Academy of Sciences, Moscow 119017, Russia

ARTICLE INFO

Article history:
Received 19 July 2016
Received in revised form 22 November 2016
Accepted 13 December 2016
Available online 15 December 2016

Keywords:
Dust
Boundary layer meteorology
Air quality
Heterogeneous reaction
WRF-Chem

ABSTRACT

An online coupled meteorology-chemistry-aerosol model (WRF-Chem) is used to quantify the impact of soil dust on radiative forcing, boundary layer meteorology and air quality over East Asia. The simulation is conducted from 14 to 17 April 2015, when an intense dust storm originated in the Gobi Desert and moved through North China. An integrated comparison analysis using surface observations, satellite, and lidar measurements demonstrates the excellent performance of the WRF-Chem model for meteorological parameters, pollutant concentrations, aerosol optical characteristics, and the spatiotemporal evolution of the dust storm. The maximum aerosol optical depth induced by dust aerosols is simulated to exceed 3.0 over the dust source areas and 1.5 over the downwind regions. Dust has a cooling effect (-1.19 W m^{-2}) at the surface, a warming effect ($+0.90$ W m^{-2}) in the atmosphere and a relatively small forcing (-0.29 W m^{-2}) at the top of the atmosphere averaged over East Asia from 14 to 17 April 2015. Due to the impact of dust aerosols, the near-surface air temperature is decreased by 0.01 °C and 0.06 °C in the daytime and increased by 0.13 °C and 0.14 °C at night averaged over the dust sources and the North China Plain (NCP), respectively. The changes in relative humidity are in the range of -0.38% to $+0.04\%$ for dust sources and -0.40% to $+0.27\%$ for NCP. The maximum decrease in wind speed of ~0.1 m s^{-1} is found over NCP. The planetary boundary layer height during the daytime exhibits maximum decreases of 16.34 m and 41.70 m over dust sources and NCP, respectively. The pollutant concentrations are significantly influenced by dust-related heterogeneous chemical reactions, with a maximum decrease of 1.66 ppbV for SO_2, 7.15 ppbV for NO_y, 35.04 μg m^{-3} for NO_3^-, and a maximum increase of 9.47 μg m^{-3} for SO_4^{2-} over the downwind areas.

1. Introduction

Soil dust has gained increasing attention in recent decades, because it not only affects energy budget of climate system by scattering and absorbing radiation, but also has an adverse effect on air quality and human health (Liu et al., 2003; Kutiel and Furman, 2003; Yu et al., 2011; Han et al., 2012; Liu et al., 2016; Maghrabi and Al-Dosari, 2016). Dust aerosols are mainly uplifted from arid, semiarid and desert regions, which cover approximately one third of the earth's land surface (Chun et al., 2001). The entrainment of dust and its further emission into the atmosphere depend on several factors, including vegetation cover, soil moisture, snow depth and threshold friction velocity (Andy, 2002; Kang et al., 2014). Dust aerosols can be removed by dry deposition and wet deposition from the atmosphere. Dry deposition dominates near source regions (Zhao et al., 2003; Yasunari et al., 2016), and wet deposition dominates during the long-range transport (Hsu et al., 2009). Recent estimate of global dust emission ranges from 1000 to 5000 Mt/year (Sokolik and Toon, 1996; Zender et al., 2004), with high temporal and spatial variability.

East Asia is one of the most important dust emission regions in the world. Dust particles are often observed in spring (from March to May), mainly lifted up from the Taklimakan Desert in west China and the Gobi Desert in south Mongolia and north China (Chen et al., 2015a,b). The annual dust emission ranges from 500 to 1100 *Tg* (Zhang et al., 1997), accounting for approximately 10–25% of global emissions (Tegen and Schepanski, 2009).

Extensive studies have researched the spatiotemporal evolutions of dust aerosols over East Asia, by in-situ measurements, satellite retrievals, and numerical simulations. For example, Wang et al. (2016) analyzed surface meteorological data from 319 stations in China and found the value of DSE (dust storm event, meaning the duration and outbreak area of a complete dust storm process) was decreasing under the global

* Corresponding author at: LAPC, Institute of Atmospheric Physics (IAP), Chinese Academy of Sciences (CAS), Beijing 100029, China.
E-mail address: mgzhang@mail.iap.ac.cn (M. Zhang).

http://dx.doi.org/10.1016/j.atmosres.2016.12.008
0169-8095/

warming scenarios from 1978 to 2007, but strong dust storms (the outbreak area of an event > 105 km^2) will probably bring greater risk to air quality in future. By using automated two-wavelength polarization lidar, Sugimoto et al. (2005) found that the contribution of dust aerosols to the total backscattering coefficient was >60% during dust events over urban areas in China and Japan (Shimizu et al., 2004). However, these in-situ observations are generally spatial limited for the sparse coverage of ground-based sites (Chen et al., 2015a,b). The transport and characteristics of dust storms, including the changes of atmospheric parameters along dust tracks, can be monitored by multi-satellite sensors. Cao et al. (2014) discussed aerosol optical properties during several severe dust storms from 2005 to 2010 using MODIS data. Their results show the increase of the concentration of scattering particles during dust events and the enhancement of water mass mixing ratio after dust events. Satellite observations from CALIPSO also revealed that summer-time dust storms over the Tibetan Plateau occurred more frequently than previously found from Tibetan surface observations, because few surface-layer sites were available over remote Tibet (Huang et al., 2007; Liu et al., 2008). In spite of excellent spatial coverage, satellite measurements often generated biases over cloudy areas.

As an effective method to reproduce complex physical and chemical processes, numerical modeling has been widely used to exhibit the evolution characteristics of dust storms with high temporal and spatial resolution. A number of offline simulations have been conducted to estimate the amount of dust emission and the impacts of dust aerosols on radiative forcing (Grini et al., 2005; Park et al., 2005; Ahn et al., 2007). However, these non-coupled offline simulations failed to represent the radiative effect associated with adjustments in both dust and meteorological fields (Liu et al., 2016). Chen et al. (2014) used a fully chemistry-meteorology coupled WRF-Chem model to estimate dust radiative forcing, and reported that dust decreased the net surface radiative flux by 5–30 W m^{-2}. Surface cooling could increase atmospheric stability and generate negative feedbacks on dust mobilization, leading to a decreased dust load (Zhang et al., 2009). By using an online coupled regional model RIEMS, Han et al. (2013) analyzed the changes in dust-induced meteorological variables in March 2010 over East Asia, and reported that the radiative forcing induced by dust aerosols caused a maximum reduction of temperature by −7.0 °C and wind speed by −4.0 m s^{-1}. By using the WRF-Chem model, Ying et al. (2011) revealed that dust aerosols could significantly reduce the surface-layer concentrations of OH and O_3 by influencing the solar radiation and atmospheric photolysis rate.

Different dust schemes with different physicochemical parameters result in different dust emission amounts (Kang et al., 2011; Wu and Lin, 2013). Shao (2004) proposed a dust emission parameterization, and the scheme was proved to generate reasonable dust emission amount over source areas, and have a great performance in reproducing the spatial distribution of dust particles over the downwind regions in East Asia (Wu and Lin, 2013; Kang et al., 2014; Su and Fung, 2015).

Recently, increasing attention has been focused on dust-related heterogeneous reactions (Wang et al., 2012). The laboratory studies have demonstrated the impacts of heterogeneous chemistry on the surface of dust particles on pollutant concentrations (Zhu et al., 2010; He et al., 2014). However, few modeling studies which focused on dust events over East Asia included heterogeneous chemistry on the surface of dust particles in the models. More recently, a latest severe dust storm occurred in East Asia during 14–17 April 2015. The detailed transport mechanism, radiative perturbations, and the feedback to meteorological fields during this dust event have not been estimated yet.

In this study, we use a fully-coupled Weather Research and Forecasting Model with Chemistry (WRF-Chem) model, with an advanced dust emission scheme (Shao, 2004 scheme) and nine dust-related heterogeneous chemical reactions, which were not included in WRF-Chem model previously, to obtain a comprehensive understanding of the evolutions of the latest dust storm, and quantify the impact of dust aerosols on radiative forcing, boundary layer meteorological parameters, and gaseous pollutants as well as inorganic aerosols. The manuscript is organized as follows. The descriptions of model, heterogeneous reactions, emissions, numerical simulations and observational data are presented in Section 2. The simulated meteorological parameters, pollutant concentrations, aerosol optical depth, and dust extinction coefficient are evaluated in Section 3.1. Section 3.2 exhibits the evolution of the dust episode. The impacts of dust on meteorological variables, and pollutant concentrations are presented in Sections 3.3 and 3.4, respectively. Sections 4 and 5 show the summaries and discussions.

2. Methodology and data

2.1. WRF-Chem model

The Weather Research and Forecasting Model version 3.7 (Skamarock et al., 2008) coupled with Chemistry (Grell et al., 2005) is employed to simulate the meteorology and chemistry over the model domain as shown in Fig. 1(ii). The model computational domain covers Asia (15.4°S–58.3°N, 48.5°E–160.2°E) using 180 × 170 grid points at 45 km horizontal resolution. To minimize the influence from lateral boundary conditions, the simulated results in the inner region (29.8°N–50.6°N, 79.2°E–133.3°E) with 45 × 92 grid points are selected to analyze (Wu et al., 2012). The vertical grid contains 52 full sigma levels from the surface to 50 hPa, of which the lowest sixteen layers are below 1 km, and the first layer is approximately 16 m.

The initial and lateral boundary conditions of meteorological fields are obtained from the National Center for Environmental Prediction (NCEP) Final Analysis (FNL) data with 1° × 1° spatial resolution and 6 h temporal intervals. Four dimensional data assimilation (FDDA) (Otte, 2008) is used, with a nudging coefficient of 3.0×10^{-4} for the wind, temperature and humidity at all levels, to limit the model bias of simulated meteorological fields (Lo et al., 2008). The output data from a global chemical transport model MOZART-4 is used as the chemical initial and boundary conditions. Detailed descriptions of the species mapping from MOZART to WRF-Chem can be found on the website http://www.acd.ucar.edu/wrf-chem/.

The gas-phase chemical mechanism CBMZ (Carbon Bond Mechanism) (Zaveri and Peters, 1999) coupled with an 8-bin sectional aerosol model MOSAIC (Model for Simulating Aerosol Interactions and Chemistry) (Zaveri et al., 2008) with aqueous chemistry is used in this study. The aerosol size distribution is divided into discrete size bins defined by their lower and upper dry particle diameters (Gao et al., 2015). All major aerosol species are considered in this model, including sulfate, nitrate, ammonium, chloride, sodium, black carbon, primary organic mass, liquid water and other inorganic mass (Zaveri et al., 2008). Detailed parameterization schemes used in this study are listed in Table 1.

The Shao 2004 dust emission scheme (referred to as Shao_2004) is used in our simulation. This dust emission parameterization was proposed by Shao (2004) and was implemented in WRF-Chem by Kang et al. (2011) and Wu and Lin (2013). Three important parameters are used to calculate the dust emission amounts: (1) the threshold friction velocity, (2) the horizontal sand flux, and (3) the vertical dust flux. The threshold friction velocity is defined as the minimum friction velocity to initiate soil particle movement. It can be parameterized by the cohesive force which is proportional to particle size (Shao and Lu, 2000), and it is strongly affected by soil moisture, salt concentrations in the soil, and roughness elements on the surface. The horizontal sand flux indicates the intensity of dust saltation, defined as a vertical integral of the streamwise saltating particle flux density when the friction velocity exceeds the threshold friction velocity (White, 1979). The vertical dust flux is defined as the emitted dust mass concentration per unit area per unit time, and it is calculated using the equation proposed by Shao (2004). More detailed descriptions of the dust parameterization can be found in Shao (2004) and Kang et al. (2011).

Previous studies have reported that Shao_2004 scheme had a good performance in dust emission amount over source areas and spatial

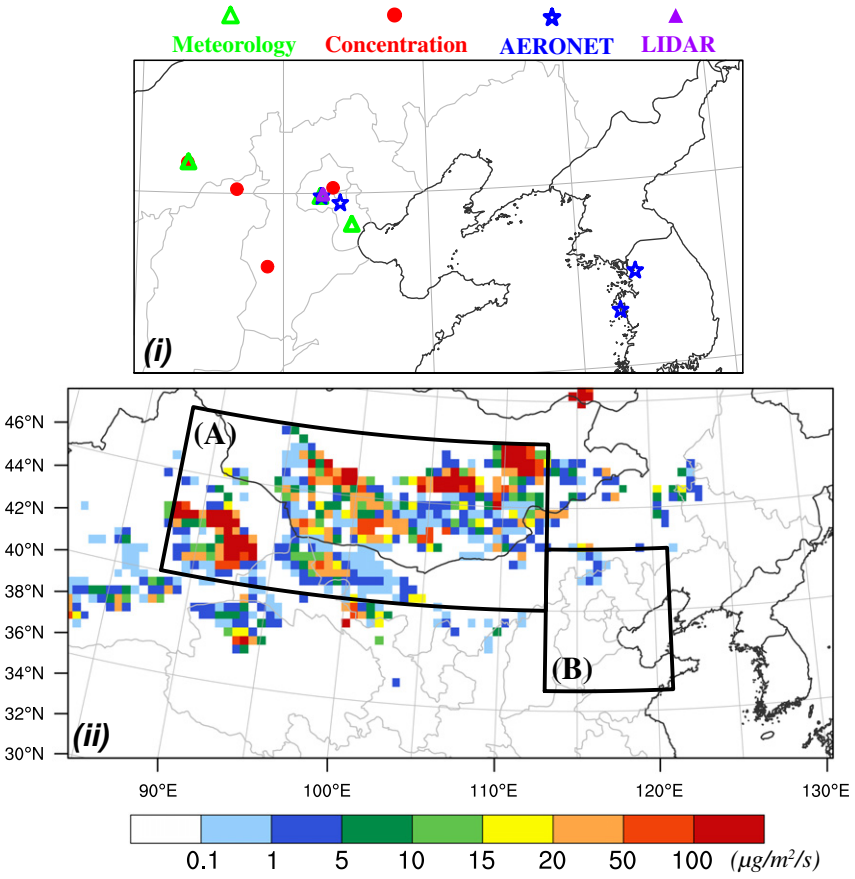

Fig. 1. (i) The locations of the observation stations. Green triangles, red dots, blue five-pointed stars, and the purple triangle represent meteorological stations, concentration sites, AERONET sites, and lidar station, respectively. (ii) Study domain and spatial distribution of dust emissions over East Asia. Two regions (A: dust source areas, B: North China Plain) are defined by the black boxes for analysis.

distribution of dust particles over the downwind regions over East Asia (Wu and Lin, 2013; Kang et al., 2014; Su and Fung, 2015). In this study, the dust scheme is coupled with the MOSAIC aerosol module following Zhao et al. (2010), who partitioned the total dust mass into eight bins in the MOSAIC model.

2.2. Heterogeneous reactions

Table 2 shows the nine heterogeneous chemical reactions that are assumed to occur on the surface of dust particles in this study. Absorption and heterogeneous reactions of gases on the dust particles are commonly parameterized using a pseudo-first-order rate constant (Zhu et al., 2010; Li et al., 2011; Wang et al., 2012; Li et al., 2012; Zheng et al., 2015), and they are assumed to be irreversible (Jacob, 2000).

Table 1
Options in the WRF-Chem model used in this study.

Options	WRF-Chem
Microphysics option	Morrison two-moment microphysics scheme
Longwave radiation option	RRTMG scheme
Shortwave radiation option	RRTMG scheme
Surface layer option	MYNN surface layer
Land surface option	Unified Noah land-surface model
Urban canopy model	Single-layer UCM
Boundary layer option	MYNN 2.5 level TKE scheme
Cumulus option	Grell 3D ensemble scheme
Photolysis scheme	Fast-J
Dust scheme	Shao (2004)
Chemistry option	CBMZ
Aerosol option	MOSAIC

The rate coefficient k_i (s^{-1}) for the loss of gaseous pollutants is calculated as proposed by Heikes and Thompson (1983):

$$k_i = \int_{r_{min}}^{r_{max}} k_{mt,i}(r) \times n(r) \times dr \quad (1)$$

where i represents the gas-phase species, $n(r) \times dr$ is the number concentration (particles cm^{-3}) of particles with a radius between r and $r + dr$ (cm), $k_{mt,i}(r)$ is the size-dependent mass transfer coefficient ($m^3\ s^{-1}$) and is determined by

$$k_{mt,i} = \frac{4 \times \pi \times D_i \times V}{1 + K_n \times \left(\chi + \frac{4 \times (1-\gamma)}{3 \times \gamma}\right)}, \quad (2)$$

where D_i ($cm^2\ s^{-1}$) is the gas-phase molecular diffusion coefficient of species i, V is the ventilation coefficient that is taken as unity, K_n is the dimensionless Knudsen number which is defined as the ratio of the effective mean free path of a gas molecule in air to the effective particle radius, and χ represents a correction factor for anisotropic movement. The reactive uptake coefficient γ represents the fraction of collisions with dust particles that lead to irreversible loss of gases, and it is the most important parameter for $k_{mt,i}$. However, the uncertainty of γ is very large (Michel et al., 2002; Wang et al., 2012; Kumar et al., 2014). Our study is focused on dust aerosols over East Asia, and the best guess values of γ for different gases are taken from Zhu et al. (2010) and Kumar et al. (2014), as shown in Table 2. Many laboratory studies have demonstrated the importance of relative humidity (RH) to γ, but few modeling studies considered the dependence of γ on RH (e.g., Dentener et al., 1996; Wang et al., 2012). In this study, we include the RH-dependence

Table 2
Uptake coefficients for heterogeneous reactions on dust surfaces.

Reactions	Uptake coefficients	RH-dependence ref	Reaction ref
O_3 + Dust = Products	RH-dependence	Cwiertny et al. (2008)	Zhu et al. (2010)

HNO_3 + Dust = 0.5NO_x + ProductsRH-dependenceLiu et al. (2008)Kumar et al. (2014)OH + Dust = 0.05H_2O_2 + ProductsRH-dependenceBedjanian et al. (2013a)Kumar et al. (2014)HO_2 + Dust = 0.1H_2O_2 + ProductsRH-dependenceBedjanian et al. (2013b)Kumar et al. (2014)H_2O_2 + Dust = Products2.00E−03–Pradhan et al. (2010)NO_2 + Dust = 0.5HONO + 0.5$HNO_3$2.10E−06–Zhu et al. (2010)NO_3 + Dust = $HNO_3$0.1–Martin et al. (2003)N_2O_5 + Dust = 2$HNO_3$0.03–Zhu et al. (2010)SO_2 + Dust = H_2SO_4RH-dependencePreszler Prince et al. (2007)Zheng et al. (2015)

of γ for gases (e.g., SO_2, O_3, OH, HO_2 and HNO_3), as in Kumar et al. (2014).

2.3. Emissions

The anthropogenic emissions are taken from the MIX inventory (mosaic Asian anthropogenic emission inventory for MICS-Asia and HTAP projects, http://mix.greenresource.cn/) for year 2010. The species include sulfur dioxide (SO_2), nitrogen oxides (NO_X), carbon monoxide (CO), non-methane volatile organic compounds (NMVOC), ammonia (NH_3), black carbon (BC), organic carbon (OC), $PM_{2.5}$ (particle matter with an aerodynamic diameter of 2.5 μm or less), PM_{10} (particle matter with an aerodynamic diameter of 10 μm or less), and carbon dioxide (CO_2) aggregated from four sectors (power, industry, residential, and transportation). The biogenic emissions are calculated online using the Model of Emission of Gases and Aerosol from Nature (MEGANv2.04). The biomass burning emissions are taken from the Global Fire Emissions Database, Version 3 (GFEDv3.1). The volcano emissions are taken from AEROCOM hindcast data and the Japan Meteorological Agency. Dust emission is calculated using the algorithm proposed by Shao (2004), and sea salt emission is calculated online following Gong et al. (1997).

2.4. Numerical experiments

Two dust events were recorded by China's National Weather Bureau from 15 March to 19 April 2015, which swept through northern China on 28 March and 15 April, respectively. Although the second dust storm only lasted for two days, it was regarded as the worst sandstorm event over the past decade, with PM_{10} mass concentrations at most monitoring sites in Beijing reaching 1000 μg m^{-3}.

Our simulation is conducted for the period over 10 to 18 April 2015 with the hourly model output. The initial four days are discarded as model spin up to minimize the effect of the initial conditions. To quantify the impacts of dust aerosols and heterogeneous chemical reactions, we perform the following three WRF-Chem simulations (Table 3): (1) CTL: The control simulation with dust emissions and heterogeneous chemical reactions on dust surface; (2) NoD_NoH: The simulation without dust emissions and heterogeneous chemical reactions on dust surface; (3) D_NoH: The simulation with dust emissions but without heterogeneous chemical reactions on dust surface. The results from CTL simulation during 14–17 April 2015 are used to evaluate the model performance and exhibit the spatiotemporal evolutions of the dust storm. The impacts of dust aerosols on radiative forcing and planetary boundary-layer meteorology can be quantified by (D_NoH – NoD_NoH). The differences between D_NoH and CTL simulations represent the effects of dust-related heterogeneous chemical reactions on air quality.

2.5. Observation data

The simulated meteorological parameters, including 2 m temperature (T_2), 2 m relative humidity (RH_2), and 10 m wind speed (WS_{10}), are compared with hourly measurements at three sites (Hohhot (40.82°N, 111.68°E), Beijing (39.93°N, 116.28°E) and Tianjin (39.18°N, 117.35°E)) in China collected from the website http://www.wunderground.com. The hourly measurements of surface-layer concentrations for SO_2, NO_2, $PM_{2.5}$ and PM_{10} at four Chinese stations (Hohhot (40.80°N, 111.66°E), Beijing (40.14°N, 116.72°E), Shijiazhuang (38.05°N, 114.45°E) and Shanxi (40.11°N, 113.38°E)) are provided by the China National Environmental Monitoring Center (CNEMC) (http://113.108.142.147:20035/emcpublish/). The observed hourly mass concentrations for sulfate and nitrate are taken from the Research Center for Eco-Environmental Sciences (RCEES), Chinese Academy of Sciences (CAS) (located at 40.01°N, 116.34°E). The Aerosol Robotic Network (AERONET), a ground-based remote-sensing aerosol network consisting of worldwide automatic sun- and sky-scanning spectral radiometers (Holben et al., 1998), provides the aerosol optical depth (AOD) products at 440 and 675 nm, which are used to calculate the AOD at 550 nm with the Angström exponent. The measured AOD values at four sites (Beijing_CAMS (39.93°N, 116.32°E), Xianghe (39.75°N, 116.96°E), Anmyon (36.54°N, 126.33°E) and Yonsei_Univ (37.56°N, 126.94°E)) are used, and AERONET Level 1.5 data (cloud-screened data) are utilized in this study because Level 2.0 data (cloud-screened and quality-assured data) are not available during the simulation period. The satellite-retrieved 550 nm AOD products from the Moderate Resolution Imaging Spectroradiometer (MODIS) are also used to compare with the simulated ones. The model results from 10:00 to 11:00 (LST) are extracted and averaged, because MODIS on board the Terra platform passes over China at 10:30 local time. The time-height cross-sections of the dust extinction coefficient observed by Mie-lidar system are used to evaluate the vertical distribution and temporal evolution of simulated dust aerosols. The lidar has a vertical resolution of 30 m and covers from the surface to 3 km, and it is located at the Institute of Atmospheric Physics (IAP), Chinese Academy of Sciences (CAS) (39.98°N, 116.38°E). All observation sites mentioned above are marked in Fig. 1(i).

3. Results

3.1. Model evaluation

Simulation results from the CTL scenario from 14 to 17 April 2015 are used to compare with observations for evaluating the model performance, including meteorological parameters (T_2, RH_2, WS_{10}), air pollutant concentrations (SO_2, NO_2, $PM_{2.5}$, PM_{10}, NO_3^-, SO_4^{2-}) and aerosol optical properties (AOD and extinction coefficient).

Table 3
Experimental design.

Experiments	Description	Dust	Heterogeneous chemical reactions on dust surfaces
CTL[a]	Dust_Hetrxn	On	On
NoD_NoH[b]	Nodust_Nohetrxn	Off	Off
D_NoH[c]	Dust_Nohetrxn	On	Off

[a] The simulation with both dust emissions and heterogeneous chemical reactions on dust surfaces.
[b] The simulation without dust emissions and heterogeneous chemical reactions on dust surfaces.
[c] The simulation with dust emissions but without heterogeneous chemical reactions on dust surfaces.

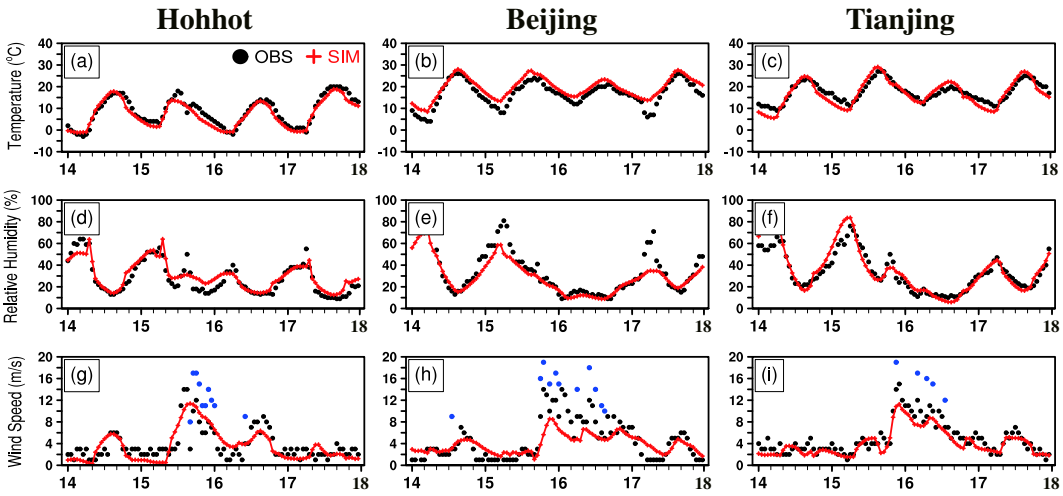

Fig. 2. Time series of the observed (black dot) and simulated (red plus) hourly 2 m temperature (°C), 2 m relative humidity (%), and 10 m wind speed (m s^{-1}) at Hohhot, Beijing, and Tianjin stations during 14–17 April 2015. Observed maximum instantaneous wind speeds are also shown as blue dots.

3.1.1. Meteorology

Fig. 2 presents the time series of simulated and observed T_2, RH_2, and WS_{10} at three sites (Hohhot, Beijing, and Tianjin) during 14–17 April 2015. The corresponding statistical metrics are listed in Table 4. As shown in Fig. 2, the model captures well the peaks and troughs of the observed T_2 (a–c) and RH_2 (d–f) at all three sites, with high correlation coefficients (R) of 0.93–0.96 for T_2 and 0.92–0.95 for RH_2. The maximum mean biases (MB) of T_2 (2.82 °C) and RH_2 (−5.83%) are found at Beijing station, which results from the overestimate of the minimum temperature and underestimate of the maximum relative humidity. The simulated wind speed, an important factor for wind erosion, generally matches well with the observations (Fig. 2g–i). However, underestimate of WS_{10} is found during 15–16 April when high wind speed is observed, which may be partly attributed to the coarse model resolution (Liu and Westphal, 2001). Meanwhile, different planetary boundary layer parameterizations produce different wind speeds (Kwun et al.,

Table 4
Statistics of the comparisons between the simulated and observed 2 m temperature (°C), 2 m relative humidity (%), 10 m wind speed (m s^{-1}), $PM_{2.5}$ (μg m^{-3}), PM_{10} (μg m^{-3}), SO_2 (ppbV) and NO_2 (ppbV) during 14–17 April 2015.

Mete_Vars	Stations	OBS[a]	SIM[a]	MB[b]	RMSE[c]	R[d]	IOA[e]
T_2 (°C)	Hohhot	8.57	7.35	−1.22	2.17	0.96	0.97
	Beijing	16.72	19.54	2.82	3.29	0.96	0.91
	Tianjin	17.49	16.96	−0.52	2.44	0.93	0.95
RH_2 (%)	Hohhot	28.04	30.18	2.14	6.61	0.92	0.94
	Beijing	35.36	29.53	−5.83	10.77	0.96	0.92
	Tianjin	33.66	35.75	2.09	7.85	0.95	0.96
WS_{10} (m s^{-1})	Hohhot	3.70	3.52	−0.18	1.96	0.76	0.87
	Beijing	4.61	3.95	−0.66	2.51	0.84	0.76
	Tianjin	4.92	4.13	−0.79	1.48	0.91	0.92
$PM_{2.5}$ (μg m^{-3})	Hohhot	55.81	49.53	−5.73	31.46	0.44	0.65
	Beijing	76.97	103.33	24.78	48.45	0.69	0.78
	Shijiazhuang	78.56	111.11	32.71	49.85	0.46	0.55
	Shanxi	42.37	64.04	21.39	33.31	0.63	0.70
PM_{10} (μg m^{-3})	Hohhot	215.05	136.83	−79.69	217.47	0.63	0.63
	Beijing	165.56	168.79	6.35	136.37	0.75	0.77
	Shijiazhuang	211.33	206.24	−3.38	105.37	0.50	0.70
	Shanxi	145.19	140.88	−9.13	64.84	0.87	0.91
SO_2 (ppbV)	Hohhot	10.83	9.78	−0.95	8.11	0.57	0.75
	Beijing	3.96	11.64	7.56	10.45	0.45	0.46
	Shijiazhuang	15.21	21.19	5.62	11.02	0.54	0.68
	Shanxi	10.53	17.86	7.46	10.10	0.82	0.72
NO_2 (ppbV)	Hohhot	21.00	18.86	−2.05	6.67	0.86	0.91
	Beijing	25.04	17.80	−7.08	13.89	0.70	0.79
	Shijiazhuang	22.54	19.91	−3.49	16.26	0.46	0.60
	Shanxi	14.37	13.58	−0.68	9.05	0.53	0.73

Where SIM_i and OBS_i indicate model predictions and observations, respectively. i refers to a given time and nstd is the total number of samples. $\overline{SIM} = \frac{1}{nstd} \times \sum_{i=1}^{nstd} SIM_i$, $\overline{OBS} = \frac{1}{nstd} \times \sum_{i=1}^{nstd} OBS_i$.

[a] OBS and SIM are the hourly averages of the observation and model results.

[b] MB is the mean bias, $MB = \sum_{i=1}^{nstd}(SIM_i - OBS_i)/nstd$.

[c] RMSE is the root mean square error, $RMSE = \sqrt{\sum_{i=1}^{nstd}(SIM_i - OBS_i)^2/nstd}$.

[d] R is the correlation coefficient, $R = \frac{\sum_{i=1}^{nstd}[(OBS_i - \overline{OBS}) \times (SIM_i - \overline{SIM})]}{\sqrt{\sum_{i=1}^{nstd}(OBS_i - \overline{OBS})^2 \times \sum_{i=1}^{nstd}(SIM_i - \overline{SIM})^2}}$.

[e] IOA is the index of agreement, $IOA = 1 - \frac{\sum_{i=1}^{nstd}(SIM_i - OBS_i)^2}{\sum_{i=1}^{nstd}(|OBS_i - \overline{OBS}| + |SIM_i - \overline{SIM}|)^2}$.

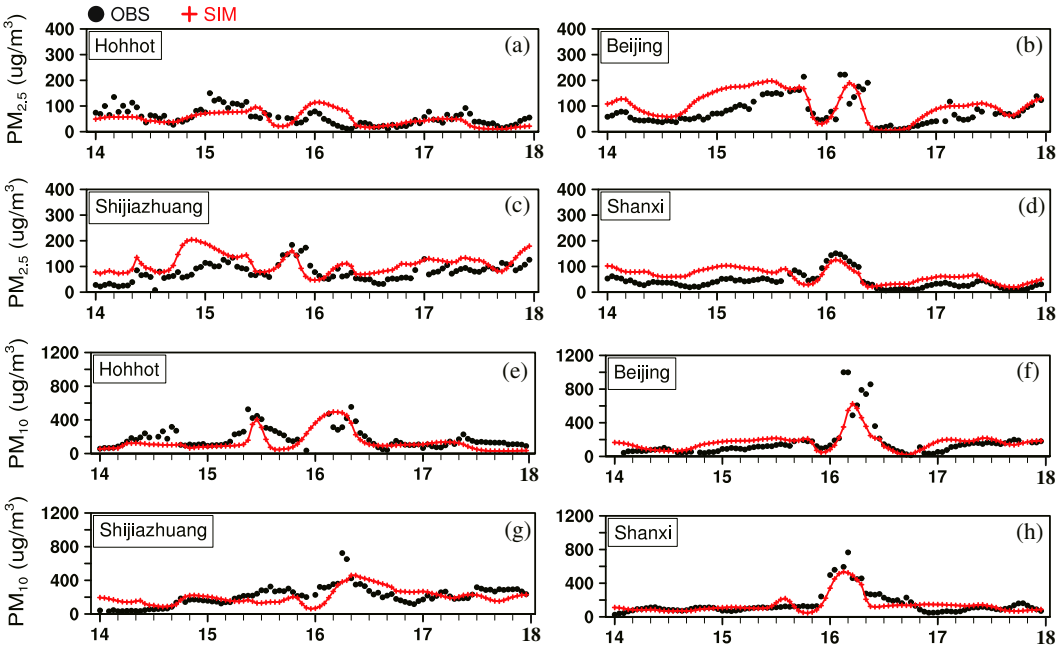

Fig. 3. Time series of the observed (black dot) and simulated (red plus) hourly $PM_{2.5}$ and PM_{10} concentrations (μg m^{-3}) at Hohhot, Beijing, Shijiazhuang, and Shanxi stations during 14–17 April 2015.

2009) and the setting of the boundary layer scheme can result in the mismatch of the wind speed between observations and simulations. This deviation can also be found in other studies (Santos-Alamillos et al., 2015; Koletsis et al., 2016). The root mean square errors (RMSE) at the three sites range from 1.48 m s^{-1} to 2.51 m s^{-1} and the correlation coefficients range from 0.76 to 0.91. We also present observed maximum instantaneous wind speed in Fig. 2(g—i) with blue dots, indicating the eruption of a dust storm. The index of agreement (IOA) is a standardized measure of model prediction error, varying between 0 and 1. A value of 1 indicates a perfect match, and 0 indicates no agreement (Willmott, 1981). Table 4 exhibits high IOA values of exceeding 0.75 for T_2, RH_2 and WS_{10}, indicating excellent performance of WRF-Chem in simulating meteorological parameters.

3.1.2. Particle matter and gas-phase pollutants

The surface-layer concentrations of $PM_{2.5}$, PM_{10}, SO_2 and NO_2 from 14 to 17 April 2015 are collected at four Chinese sites: Hohhot (near the dust source region), Beijing, Shijiazhuang, and Shanxi (along the transport and downwind regions). The time series of the observed and simulated hourly $PM_{2.5}$ and PM_{10} concentrations at the four stations are shown in Fig. 3, with the statistical parameters listed in Table 4. The model successfully reproduces the general variation features of

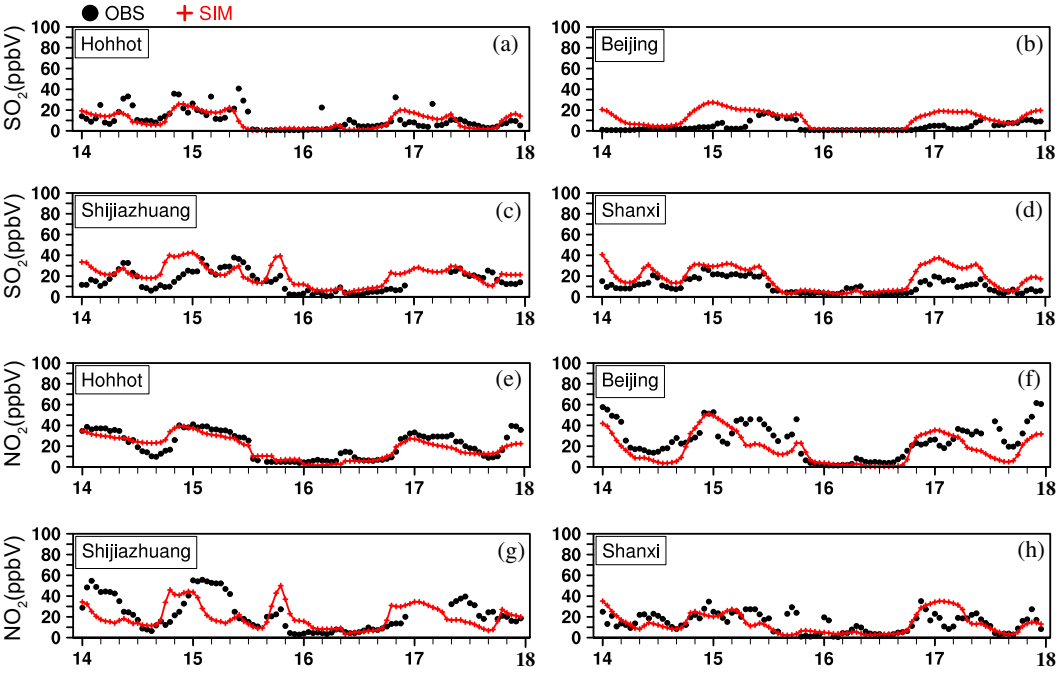

Fig. 4. Time series of the observed (black dot) and simulated (red plus) hourly SO_2 and NO_2 mixing ratios (ppbV) at Hohhot, Beijing, Shijiazhuang, and Shanxi stations during 14–17 April 2015.

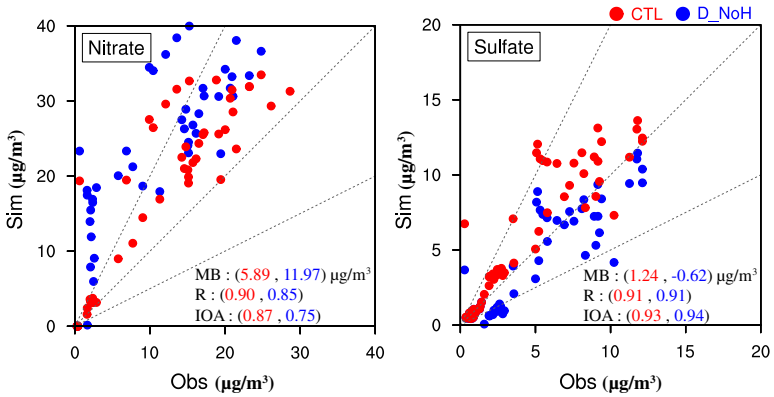

Fig. 5. Scatter plots of the observed and simulated hourly nitrate and sulfate concentrations (μg m^{-3}) at RCEES (40.01°N, 116.32°E). Red and blue dots represent simulated concentrations in CTL and D_NoH, respectively. Also shown are the 1:1, 1:2, and 2:1 lines (dashed).

aerosol concentrations at all sites during 14–17 April (IOA ranging from 0.55 to 0.91, and R ranging from 0.44 to 0.87), with high PM concentrations during dust-storm period and low PM concentrations during non-dust period. The model has acceptable performance on $PM_{2.5}$ and PM_{10} concentrations at Hohhot site near the dust source. The dust event during 15–16 April is captured by both observation and simulation. The MBs of $PM_{2.5}$ and PM_{10} are calculated to be −5.73 μg m^{-3} and −79.69 μg m^{-3}, respectively. The negative deviations at Hohhot site which is near the dust source regions may result from the model's disability to distinguish between desert and other underlying surfaces owing to the relatively coarse resolution. The model also exhibits excellent performance over the downwind areas (Beijing, Shijiazhuang, and Shanxi sites), reproducing well the temporal evolutions of PM and depicting accurately the abrupt increase in the PM_{10} concentrations that occurred on 16 April although the peak values at all the three sites (652.70 μg m^{-3}, 459.05 μg m^{-3}, and 534.82 μg m^{-3} for Beijing,

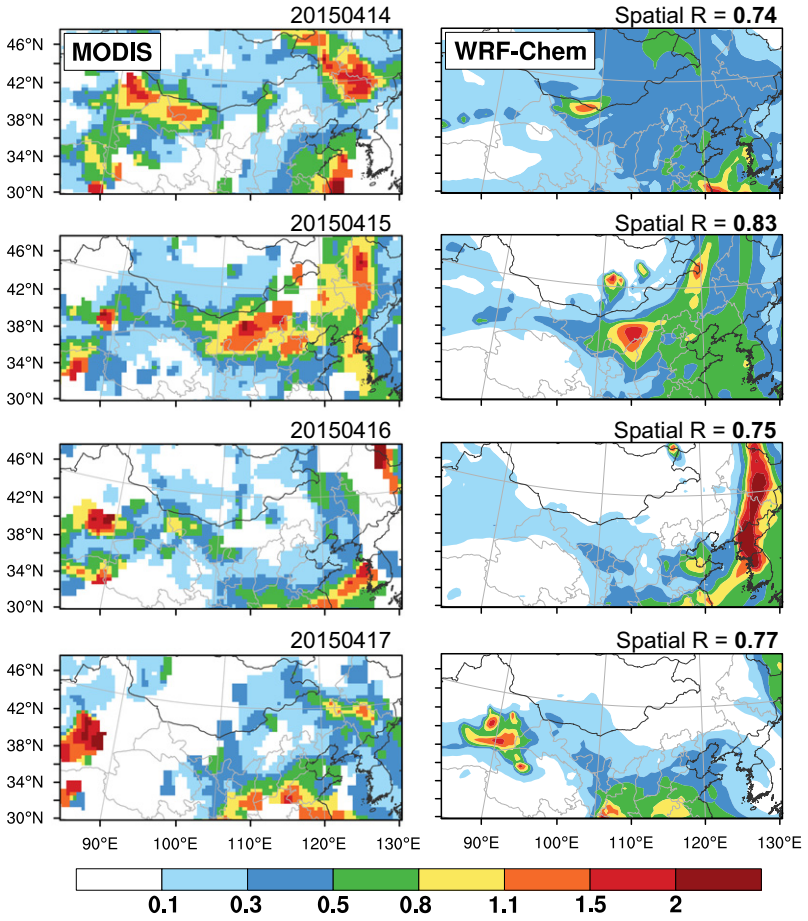

Fig. 6. Spatial distributions of the aerosol optical depth (AOD) at 550 nm retrieved from MODIS (left) and simulated by WRF-Chem model (right) during 14–17 April 2015. The MODIS retrievals are a combination of the standard (over ocean) and "Deep Blue" (over land) products. Unit: —.

Shijiazhuang, and Shanxi sites respectively) are underestimated. The underestimated maximum WS_{10} may account for the underestimation of the peak values of PM_{10} concentrations.

Fig. 4 shows the time series of the observed and simulated hourly SO_2 (a–d) and NO_2 (e–h) mixing ratios. The dust event started on 15 April with high surface-layer wind speed, decreasing the mixing ratios of SO_2 and NO_2, and ended on 17 April with increasing SO_2 and NO_2 concentrations. Despite an overestimation for SO_2 (MBs ranging from −0.95 to 7.56 ppbV) and an underestimation for NO_2 (MBs ranging from −0.68 to −7.08 ppbV) (Table 4), the model generally captures well the temporal evolutions of the two gases at all stations, with high R values of 0.45–0.86 and IOA values of 0.46–0.91.

The simulated hourly concentrations of nitrate and sulfate from two cases (CTL and D_NoH) are compared with the observations taken from RCEES during 14–17 April (Fig. 5). The CTL simulation demonstrates that the WRF-Chem model reproduces well the observed nitrate and sulfate concentrations within a factor of 2. The R_s are calculated to be 0.90 and 0.91, and IOAs are 0.87 and 0.93 for nitrate and sulfate, respectively. Comparing the concentrations in D_NoH and CTL simulations, we find that the simulation for nitrate with heterogeneous chemistry on dust surface is improved significantly, with the MB decreasing from 11.97 μg m^{-3} to 5.89 μg m^{-3}. The WRF-Chem exhibits excellent performance on sulfate concentrations, with a MB value of 1.24 μg m^{-3} in CTL simulation).

3.1.3. Aerosol optical depth

The spatial distributions of AOD at 550 nm simulated by the WRF-Chem model and retrieved from MODIS are shown in Fig. 6. The model generally reproduces well the spatial patterns and temporal evolutions of AOD. On 14 April, both the observed and simulated AOD values reflect the generation of dust particles over the Taklimakan Desert. The high AOD values retrieved from MODIS over northeast China are mainly attributed to haze particles. The haze phenomenon can be detected from the product of the aerosol subtypes of CALIPSO (the Cloud-Aerosol Lidar and Infrared Pathfinder Satellite Observations) instruments, as well as the aerosol index from OMI (Ozone Monitoring Instrument). The failure to capture the haze may partly result from the non-real-time emission inventory; the emissions used in this study are for year 2010. On 15 April, the modeled AOD captures the spatial distribution but slightly underestimates the values in northern China. On 16 April, large AOD values are shown by WRF-Chem model, stretching from northeast China to the Korean Peninsula and the Yangtze River Delta. However, these large values are mainly contributed by thick clouds. Due to cloud contamination, the AOD values are set to be missing by MODIS, but the large cloud water content makes a maximum AOD value >2 in simulation results. Other than dust aerosol, anthropogenic aerosol is also a main contributor to AOD values on 17 April. At the same time, another local dust event occurred in the Taklimakan Desert and was also captured by the WRF-Chem model. Fig. 7 shows the scatter plots of hourly AOD values at 550 nm taken from AERONET and simulated by the model for four sites from 14 to 17 April 2015. The model generally has a good performance on AOD values. The correlation coefficients are in the range of 0.78–0.96, and the MBs are in the range of 0.06–0.31.

3.1.4. Dust extinction coefficient

Mineral dust can be discerned according to the depolarization ratio (DR) of their scattering light signal. Based on the characteristic, the dust extinction coefficients can be calculated according to DR and used to estimate and validate the temporal evolutions of dust storms. Fig. 8 shows the dust extinction coefficients in Beijing measured by lidar and simulated by the model. Both the measured and simulated time-height cross-sections clearly exhibit the dust plumes from 15 to 16 April. However, the model generally underestimates the extinction coefficient values, especially on 16 April. The mismatch may be partly attributed to the negative deviation of PM_{10} concentrations as shown in Fig. 3(f).

In summary, all the above validations suggest that the WRF-Chem model has the ability to reproduce the temporal evolutions and spatial distributions of the severe dust storm that occurred on 15 April, which provides confidence for further investigation with the model.

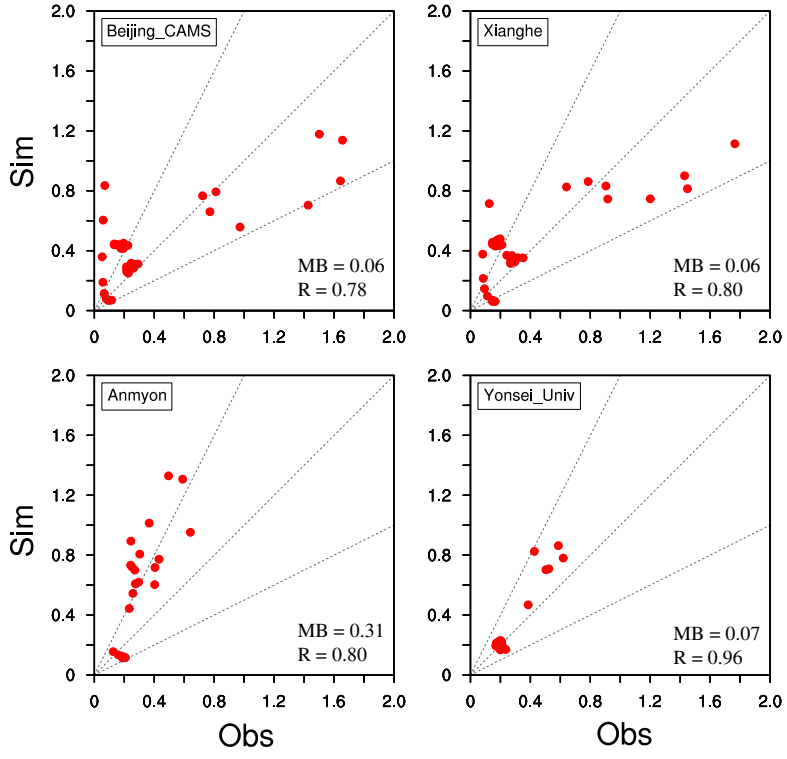

Fig. 7. Scatter plots of the observed and simulated hourly AOD at Beijing_CAMS, Xianghe, Anmyon, and Yonsei_Univ sites. Also shown are the 1:1, 1:2, and 2:1 lines (dashed). Unit: —.

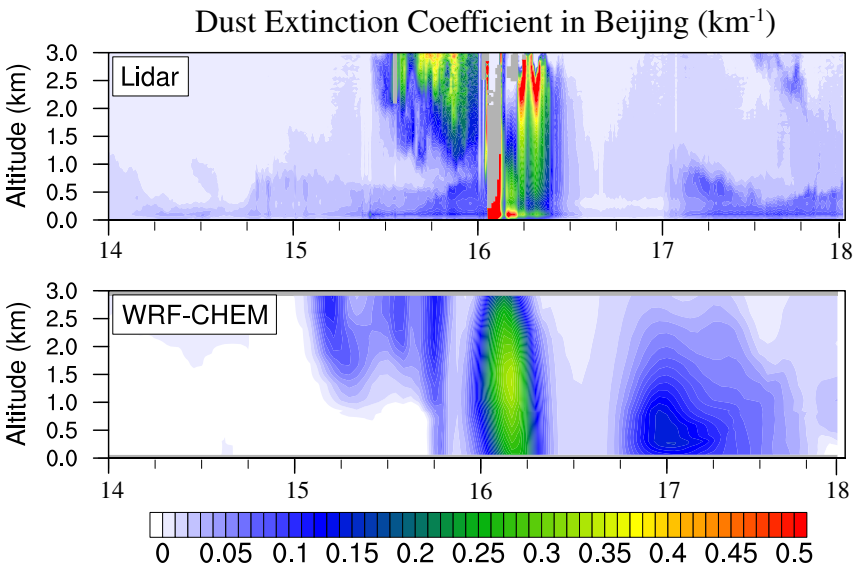

Fig. 8. Time-height cross-sections of the dust extinction coefficients measured from Mie-lidar and simulated by WRF-Chem at IAP (39.98°N, 116.38°E) during 14–17 April 2015. The simulated dust extinction coefficient is calculated as the difference in extinction coefficients in NoD_NoH and D_NoH simulations. Unit: km^{-1}.

3.2. Dust episode

Mineral dust makes a significant contribution to AOD during dust events (Han et al., 2012). Therefore, the AOD values at 0400 and 1600 (LST) from 14 to 17 April 2015 are used to provide detailed information on the dust evolutions (Fig. 9). The dust storm occurred as follows: dust particles were first lifted up from the Taklimakan Desert at 0400 (LST) 14 April and blown eastward to northern Inner Mongolia with the

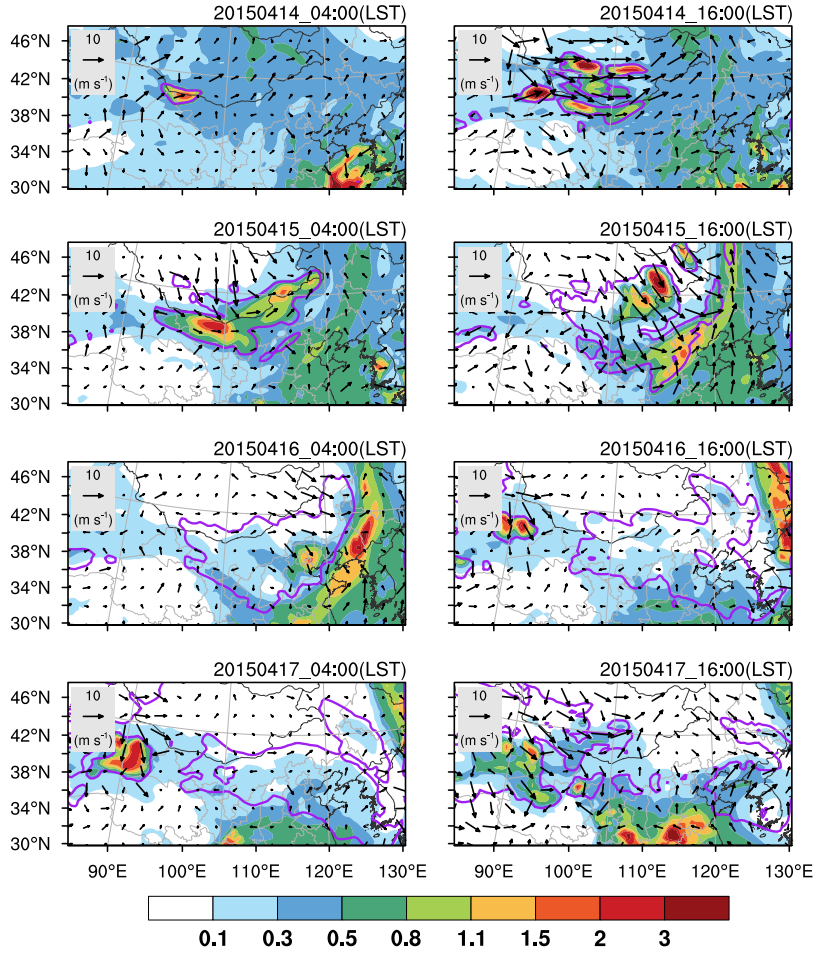

Fig. 9. Simulated spatial distributions of 10 m wind ($m\,s^{-1}$) and AOD values (—) at 0400 and 1600 (LST) from 14 to 17 April 2015. Purple contour lines denote the 50% contribution of dust aerosols to AOD.

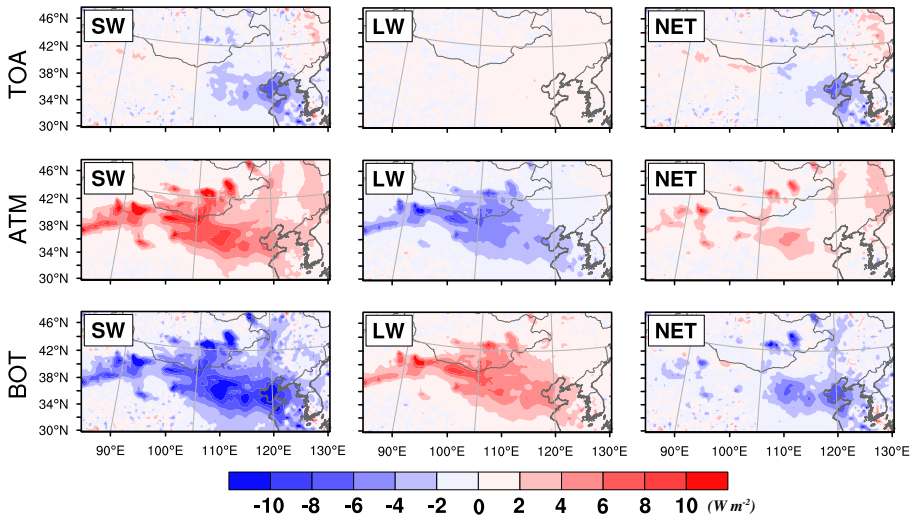

Fig. 10. Simulated all-sky radiative forcing by dust aerosols averaged over 14–17 April 2015. "TOA", "ATM", and "BOT" represent the dust radiative forcing at the top of the atmosphere, in the atmosphere, and at the surface, respectively. "NET" denotes the sum of dust shortwave (SW) and longwave (LW) radiative forcing. Unit: W m^{-2}.

increasing westerly at 1600 (LST) 14 April. A deep low-pressure system with a cold center at 850 hPa was found over northwestern Mongolia and moved to central Mongolia on 14 April. The strong temperature gradient caused a high surface-layer wind speed exceeding 10 m s^{-1}, leading to high dust concentrations of exceeding 10,000 μg m^{-3} around the Gobi Desert in Mongolia. However, most dust particles were settled near the dust sources owing to gravity. The low-pressure system continued to move eastward, and the northwesterly was predominant over the dust source regions in Mongolia at 0400 (LST) 15 April. At 1600 (LST), one trough axis stretched across northeastern China followed by a strong cold advection, resulting in additional wind erosion in southern Mongolia. The maximum instantaneous wind speed exceeded 15 m s^{-1}, which led to a movement of numerous dust particles from Mongolia to Inner Mongolia. During the late afternoon on 15 April and the following early morning, dust aerosols swept through Beijing, causing high AOD values of exceeding 1.1 at 0400 (LST) 16 April. Meanwhile, the low-pressure system persistently moved eastward, further weakening the northwesterly and decreasing the wind speed (less than the threshold velocity for dust emissions). Owing to the dry deposition, the AOD values contributed by dust aerosols decreased (<0.5) in North China from 1600 (LST) 16 April to 1600 (LST) 17 April. Although high dust concentrations were found over the Taklimakan Desert during this time, this newborn dust event was local and had a smaller effect.

3.3. Impacts of dust aerosols on radiative forcing and meteorological variables

Dust aerosols affect energy budget by scattering and absorbing radiation, and the feedback of radiative perturbations may further influence meteorological fields. Fig. 10 shows the spatial distributions of shortwave (SW), longwave (LW) and net (SW + LW) radiative forcing (RF) induced by dust aerosols at the top of the atmosphere (TOA), in the atmosphere (ATM), and at the surface (BOT) averaged over 14–17 April. The radiative forcing is calculated as the difference in radiation flux between NoD_NoH and D_NoH simulations. At TOA, the SW radiative perturbation depends strongly on the dust SW absorption and has a cooling effect, especially over downwind regions. The regional-averaged dust SW radiative perturbation at TOA is −0.54 W m^{-2}, and the maximum perturbation is −17.88 W m^{-2} over the downwind regions. The dust LW radiative forcing at TOA is generally small, with a regional-averaged value of 0.25 W m^{-2}. The net radiative perturbation, mostly determined by dust SW radiative forcing, has a cooling effect with a regional-averaged value of −0.29 W m^{-2}. In the atmosphere, dust particles absorb SW and warm the atmosphere, with regional-averaged SW radiative forcing of 2.41 W m^{-2} and a maximum value of 25.49 W m^{-2} over dust source areas. The dust LW radiative forcing has a maximum value in the deserts owing to the strong interactions between LW and coarse-mode dust particles that are spatially confined to the deserts because of their short lifetime and the limited distance they are carried (Zhao et al., 2011). The dust aerosols generally produce a net warming effect, with regional-averaged RF of 0.9 W m^{-2}. At the surface, dust aerosols attenuate the downward SW radiation, leading to a cooling effect with a regional-averaged value of −2.95 W m^{-2}, and trap the LW radiation emitted from the surface, resulting in a warming effect with a regional-averaged value of 1.76 W m^{-2}. The net RF by dust aerosols at the surface is calculated to be −1.19 W m^{-2}. Table 5 summaries the simulated dust radiative forcing averaged over the analyzed region. In general, the net radiative effects of dust aerosols are warming for atmosphere, and cooling for surface and TOA.

Fig. 11 shows the diurnal variations of the dust-induced changes in T_2, RH_2, WS_{10}, and PBLH averaged over the dust source area and the downwind region (NCP: North China Plain) during the period 15–16 April 2015. The dust-induced changes are denoted by the differences of meteorological parameters between NoD_NoH and D_NoH simulations. The simulated dust aerosols have a slight cooling effect in the daytime, with near-surface air temperature (08:00– 18:00 LST) decreasing by 0.01 °C and 0.06 °C averaged over the dust sources and NCP, respectively. However, the nocturnal temperature is simulated to increase by 0.13 °C and 0.14 °C averaged over the two regions. The maximum warming of 0.37 °C is found at night on 15 April over dust sources, and a comparable magnitude is found one day later over NCP. The RH_2 exhibits an increase in the daytime and a decrease at night. These changes show a contrary tendency with that of temperature, and range from −0.38% to +0.04% (−0.12% on average) over dust sources, −0.40% to +0.27% (−0.10% on average) over NCP. The overall decrease of relative humidity over both upstream and downstream areas may be related to the increase of air temperature, as well as the absorption of dust aerosols. The hydroscopic growth of dust particles can further aggravate air quality (Howell et al., 2006). As mentioned above, dust

Table 5
Summary of radiative forcing (W m^{-2}) by dust aerosols averaged over East Asia during 14–17 April 2015.

	SW	LW	NET
TOA	−0.54	0.25	−0.29
ATM	2.41	−1.50	0.90
BOT	−2.95	1.76	−1.19

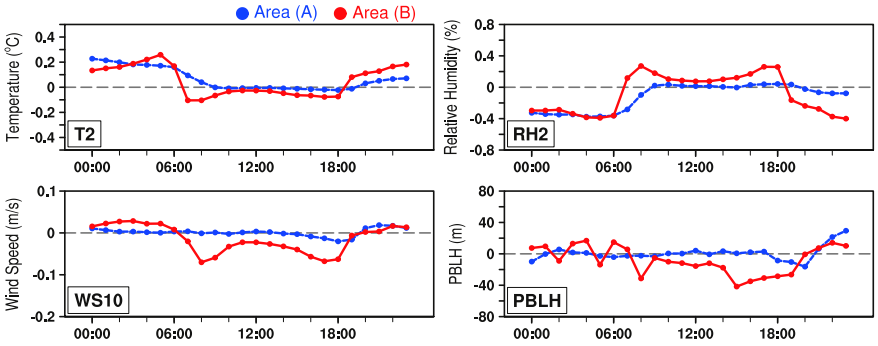

Fig. 11. Diurnal variations of the dust-induced changes in the 2 m temperature (°C), 2 m relative humidity (%), 10 m wind speed ($m\ s^{-1}$), and PBLH (m) averaged over the dust source areas (A, blue dotted line) and downwind areas (B, red dotted line) during the period 15–16 April 2015.

particles absorb solar radiation, which warms the atmosphere and cools the surface over NCP. This leads to an increase of the daytime atmospheric stability and a decrease of the wind speed near the surface with a maximum change of $-0.07\ m\ s^{-1}$. At night, dust particles trap more outgoing infrared radiation, warming the surface and cooling the atmosphere. The enhanced instability increases vertical transport of fast wind aloft to surface, by which surface wind is strengthened with a maximum change of $+0.03\ m\ s^{-1}$ over NCP. The influence of dust particles on WS_{10} over dust sources is negligible. PBLH is an important factor for turbulent mixing extent (Liu et al., 2016) and atmospheric stability (Hong, 2010). The PBLH is depressed in the daytime, with maximum decreases of 16.34 m and 41.70 m over the source areas and NCP respectively. The depressed PBLH is attributed to the lower height of capping inversion, which results from dust-induced increase of daytime atmospheric stability (Liu et al., 2016). At night, PBLH is increased owing to the dust-induced atmospheric instability; the maximum increases are 29.44 m and 16.78 m over the dust sources and NCP, respectively.

3.4. Impacts of dust aerosols on pollutant concentrations

For further analysis on the influence of dust aerosols and dust-related heterogeneous chemical reactions on pollutant concentrations, we show in Figs. 12–15 the surface-layer concentrations of gases (i.e., SO_2 and NO_y) and aerosol species (i.e., SO_4^{2-} and NO_3^-) averaged over the period of 14–17 April 2015 in NoD_NoH, D_NoH, and CTL simulations. NO_y includes NO, NO_2, NO_3, HNO_3, HONO, HNO_4, and N_2O_5, as proposed by An et al. (2013).

All the three simulations show the similar spatial distributions of surface-layer SO_2 and NO_y mixing ratios, with high values of 15–40 ppbV over downwind regions owing to high emissions and low values (<5 ppbV) near the dust source areas. The impacts of dust emissions on gases are illustrated by the differences between NoD_NoH and D_NoH simulations. Influenced by dust emissions, surface-layer SO_2 and NO_y mixing ratios are changed, especially over the downwind regions (both increase by 0.1 ppbV for SO_2 and NO_y averaged over NCP). This perturbation may result from the feedback of the influenced meteorological fields induced by dust aerosols (Gao et al., 2015), and the wind speed and PBLH decrease by $-0.02\ m\ s^{-1}$ and -4.85 m, respectively, averaged over NCP. Dust particles make the net radiation forcing negative at the surface (Table 5). As a result of surface cooling, the sensible heat flux and turbulent energy in the boundary layer decrease, leading to the reduction of PBLH and downward transport of momentum from upper layer to the surface, and consequently reduce the wind speed near the surface (Han et al., 2013; Liu et al., 2016). The differences of gas concentrations between D_NoH and CTL simulations reflect the impacts of dust-related heterogeneous chemical reactions on the gases. The simulated SO_2 and NO_y exhibit a significant response to dust-related heterogeneous chemistry, with a maximum decrease of 1.66 ppbV (29.83%) for SO_2 and 7.15 ppbV (83.59%) for NO_y over the downwind region. The reductions over dust sources are relatively smaller due to the lower concentrations of pollution gases. The differences in gas concentrations due to the combined effects of dust emission and heterogeneous chemistry (CTL minus NoD_NoH) are almost identical to those due to the effects of heterogeneous chemistry alone (CTL minus D_NoH), indicating the nonnegligible role of dust-related chemical reactions.

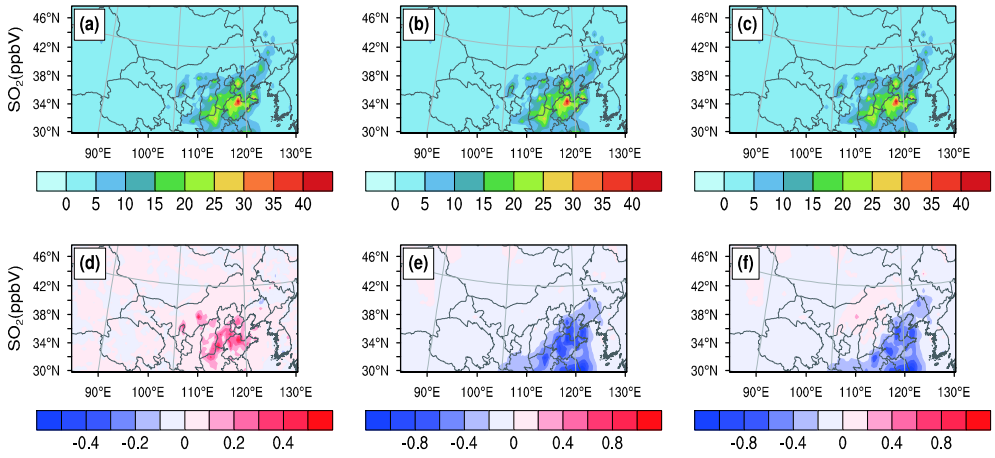

Fig. 12. Spatial distributions of the simulated SO_2 mixing ratios averaged over 14–17 April 2015 in (a) NoD_NoH, (b) D_NoH, and (c) CTL simulations. The differences in SO_2 concentrations are also shown: (d) D_NoH minus NoD_NoH, (e) CTL minus D_NoH, and (f) CTL minus NoD_NoH. Unit: ppbV.

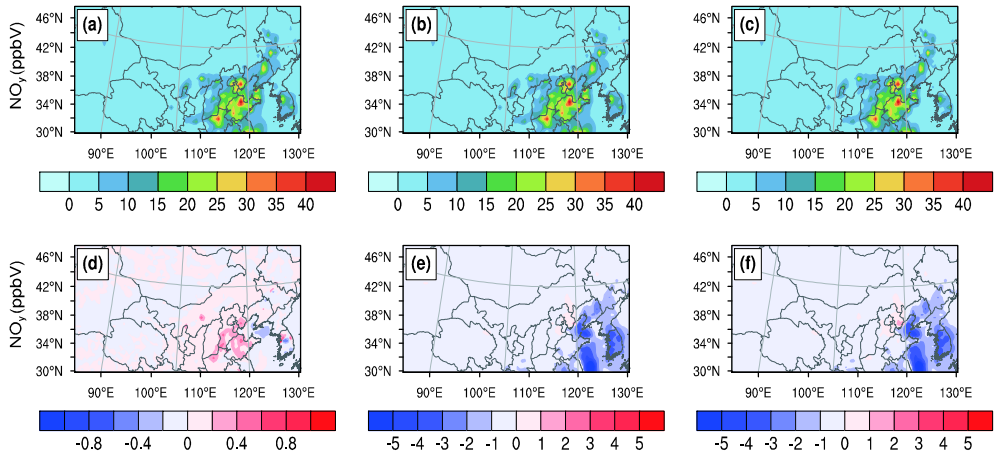

Fig. 13. Same as Fig. 12 but for the simulated NO_y. Unit: ppbV.

By comparing the concentrations of SO_4^{2-} and NO_3^- in NoD_NoH and D_NoH simulations, we find that dust emissions have a relative small effect on sulfate and nitrate. The sulfate changes by −0.42 to +0.59 μg m^{-3}, and the nitrate changes by −0.47 to +0.98 μg m^{-3} (Figs. 14 and 15). The SO_2 heterogeneous reactions on dust particles lead to a regional-averaged increase of 0.6 μg m^{-3} and a maximum increase of 9.47 μg m^{-3} for SO_4^{2-}. Although nitric acid is formed by the reactions of NO_2, NO_3, and N_2O_5 on dust particles, the concentrations of NO_3^- are decreased, owing to the uptake of nitric acid by dust aerosols. The nitrate is simulated to decrease by up to 35.04 μg m^{-3} over the downwind regions. In general, including the heterogeneous chemical reactions on dust particles in models may increase concentrations of SO_4^{2-} and decrease concentrations of NO_3^-, which improves the simulation for sulfate and nitrate in models, as previous studies have reported the underestimation of SO_4^{2-} and overestimation of NO_3^- in a lot of models (Wang et al., 2013; Gao et al., 2014; Park et al., 2014; Goto et al., 2015).

4. Conclusion

We use the online coupled WRF-Chem model to reproduce a severe dust storm occurred over East Asia from 14 to 17 April 2015 and quantify the impact of soil dust on radiative forcing, boundary layer meteorology and air quality. A variety of measurements from ground-based sites, satellite, and lidar are used to evaluate the model performance on meteorological parameters, pollutant concentrations, aerosol optical depth, and dust extinction coefficient. The model exhibits an excellent performance on these parameters and well captures the spatiotemporal evolutions of the dust storm.

The dust particles were first uplifted from the Taklimakan Desert by a deep low-pressure system and then blown eastward to northern Inner Mongolia in 14 April 2015. Due to gravity settling, most dust particles settled near the dust sources. The low-pressure system continued to move eastward, and the northwesterly was predominant over the Gobi Desert on the early morning of 15 April, which caused strong wind erosion. The dust storm exerted a widespread influence over NCP and Korean Peninsula on 16 April. The low-pressure system persistently moving eastward weakens the northwesterly and decreases the wind speed, which led to the end of the dust event on 17 April.

The regional-averaged SW and LW radiative forcing by dust aerosols at TOA are simulated to be −0.54 W m^{-2} and +0.25 W m^{-2}, respectively. The net radiative forcing at TOA has a negative value of −0.29 W m^{-2}, indicating a cooling effect of dust aerosols. The dust aerosols generally produce a net warming effect, with regional-averaged radiative forcing of 0.9 W m^{-2} in the atmosphere. At the surface, dust has a cooling effect; the net dust radiative forcing is simulated to be −1.19 W m^{-2}. In general, the net radiative effects of dust aerosols are warming for atmosphere, and cooling for surface and TOA.

Influenced by dust aerosols, T_2 is decreased in the daytime by 0.01 °C and 0.06 °C, but increased at night by 0.13 °C and 0.14 °C averaged over the dust sources and NCP, respectively. The changes in relative humidity are in the range of −0.38% to +0.04% for dust sources and −0.40% to +0.27% for NCP. The maximum decrease in wind speed of ~0.1 m s^{-1} is found over NCP, but the change is negligible over dust sources. The day-time PBLH is depressed, with the maximum decreases of 16.34 m

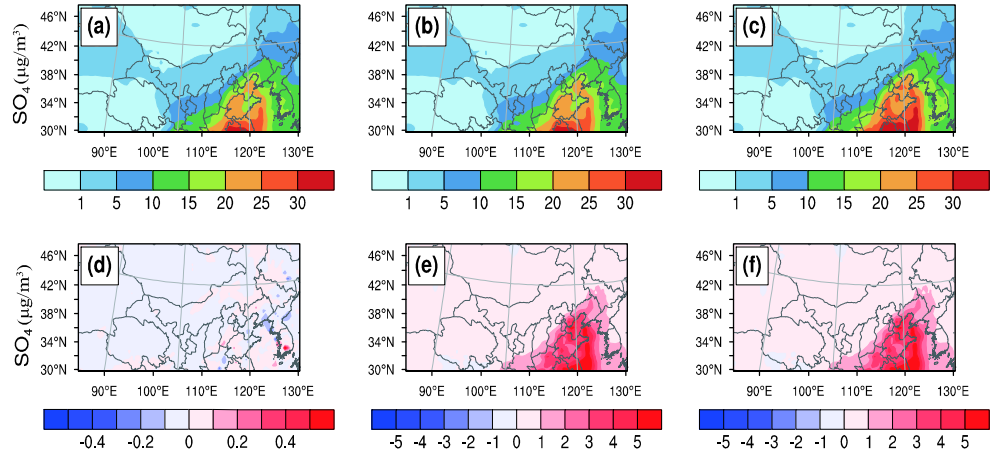

Fig. 14. Same as Fig. 12 but for the simulated SO_4^{2-}. Unit: μg m^{-3}.

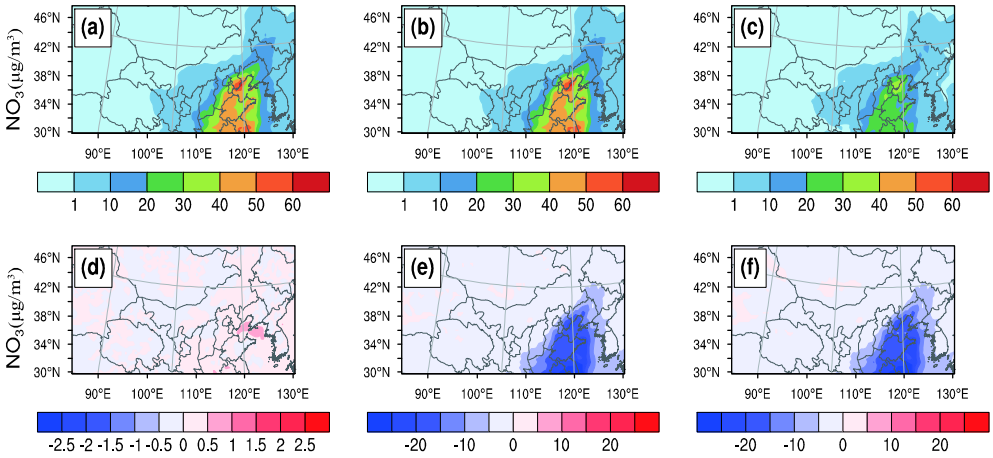

Fig. 15. Same as Fig. 12 but for the simulated NO_3^-. Unit: μg m^{-3}.

and 41.70 m over source areas and NCP, respectively. However, the PBLH increases a lot at midnight due to the dust-induced atmospheric instability.

We then examine the impacts of dust-related heterogeneous chemical reactions on the gases (SO_2, NO_y) and aerosols (SO_4^{2-}, NO_3^-). The significant reductions in SO_2 and NO_y mixing ratios are simulated over the downwind areas, with the maximum decrease of 1.66 ppbV for SO_2 and 7.15 ppbV for NO_y. The SO_2 heterogeneous reactions on dust particles lead to a regional-averaged increase of 0.6 μg m^{-3} and a maximum increase of 9.47 μg m^{-3} for SO_4^{2-}. Due to the uptake of nitric acid by dust aerosols, the nitrate exhibits a maximum decrease of 35.04 μg m^{-3} over the downwind regions.

5. Discussion

There are some uncertainties in our simulations that can be improved in future studies:

(1) The uncertainty caused by the plastic pressure of soil surface, a critical parameter used in Shao (2004), may result in lower dust emission amount (Kang et al., 2011). The accuracy of soil plastic pressure should be improved in future studies.
(2) Previous studies have reported that different uptake coefficients for heterogeneous reactions on dust surfaces may cause differences in the concentrations of gases and aerosols (Zhu et al., 2010; Wang et al., 2012; Kumar et al., 2014). Further sensitivity experiments could be conducted to quantify the differences.
(3) We just select a dust event on April 14–17, 2015 as a case study to present the influence of dust on boundary layer meteorology and air quality. Ensemble simulations with more dust events will be designed and implemented to make conclusions more robust.
(4) It is noted that the latest version of MIX is 2010 emission, while the dust storm happened in 2015. The selection of emission may intervene with the simulation results. In order to explore the influence of selected emission on the simulation results, we conduct another three simulations similar to CTL, D_NoH and NoD_NoH, but with doubled emissions. We list in Table 6 the differences in the concentrations of air pollutants averaged over NCP owing to dust and dust-related heterogeneous chemical reactions, with 2010 emissions and doubled emissions. It is found that when the anthropogenic emission doubled, the difference in the concentrations of air pollutants also nearly doubled. In fact, the ratio of the differences in the concentrations of air pollutants with 2015 emissions to those with 2010 emissions would be much smaller, because the emissions of SO_2 and NO_y only increased <5% from 2010 to 2013 (He, 2013).
(5) In this study we focus on the impacts of dust aerosols on boundary-layer meteorological parameters. The presence of mineral dust can also significantly affect the number of ice particles through heterogeneous nucleation processes (Min et al., 2014; Zhang et al., 2015), change cloud drop size distribution as cloud condensation nuclei (Posfai et al., 2013), and even influence precipitation chemistry (Dong et al., 2011). Therefore, dust-radiation-cloud-precipitation interactions will be included in future studies to provide a more thorough assessment of dust-meteorology feedback.

Acknowledgments

This work was supported by the National Basic Research Program of China (grant number 2014CB953802), the "Strategic Priority Research Program (B)" of the Chinese Academy of Sciences (grant numbers XDB05030105, XDB05030102, XDB05030103), and the Russian Scientific Fund under grant 14-47-00049. We thank Dr. Zifa Wang from Institute of Atmospheric Physics (IAP), Chinese Academy of Sciences (CAS) for providing the dust extinction coefficients, and Dr. Xiaoshan Zhang from Research Center for Eco–Environmental Sciences (RCEES), CAS for providing the nitrate and sulfate concentrations. We acknowledge the efforts of the MODIS science teams for providing the AOD retrievals and the principal investigator of AERONET for providing the AERONET

Table 6
The differences in the concentrations of air pollutants averaged over NCP owing to dust and dust-related heterogeneous chemical reactions, with 2010 emissions and doubled emissions. Unit: ppbV for SO_2 and NO_y, μg m^{-3} for SO_4^{2-} and NO_3^-.

		SO_2 (ppbV)		NO_y (ppbV)		SO_4^{2-} (μg m^{-3})		NO_3^- (μg m^{-3})	
Impacts	Description	2010	Doubled	2010	Doubled	2010	Doubled	2010	Doubled
Dust emissions[a]	Diff_1	0.10	0.21	0.10	0.19	0.01	0.02	0.12	0.25
Heterogeneous reactions[b]	Diff_2	−0.28	−0.61	−0.47	−1.14	1.23	1.69	−6.20	−13.88

[a] Dust emissions: the impacts of dust particles.
[b] Heterogeneous reactions: the impacts of heterogeneous chemical reactions on the dust surface.

data. We would like to thank Dr. Meng Gao (University of Iowa) and Dr. Chenglai Wu (IAP, CAS) for their helpful suggestions for this study. We are also very grateful to the Editor and the reviewers for their helpful comments and thoughtful suggestions.

References

Ahn, H.J., Park, S.U., Chang, L.S., 2007. Effect of direct radiative forcing of Asian dust on the meteorological fields in East Asia during an Asian dust event period. J. Appl. Meteorol. 46:1655–1681. http://dx.doi.org/10.1175/JAM2551.1.

An, J.L., Li, Y., Chen, Y., Li, J., Qu, Y., Tang, Y.J., 2013. Enhancements of major aerosol components due to additional HONO sources in the North China plain and implications for visibility and haze. Adv. Atmos. Sci. 30:57–66. http://dx.doi.org/10.1007/s00376-012-2016-9.

Andy, J.R., 2002. Dust in the earth system: the biogeochemical linking of land, air and sea. Philos. Trans. R. Soc. Lond. A 360:2905–2924. http://dx.doi.org/10.1098/rsta.2002.1096.

Bedjanian, Y., Romanias, M.N., El Zein, A., 2013a. Interaction of OH radicals with Arizona Test Dust: uptake and products. J. Phys. Chem. A 117:393–400. http://dx.doi.org/10.1021/jp311235h.

Bedjanian, Y., Romanias, M.N., El Zein, A., 2013b. Uptake of HO_2 radicals on Arizona Test Dust. Atmos. Chem. Phys. 13:6461–6471. http://dx.doi.org/10.5194/acp-13-6461-2013.

Cao, C.X., Zheng, S., Singh, R.P., 2014. Characteristics of aerosol optical properties and meteorological parameters during three major dust events (2005–2010) over Beijing, China. Atmos. Res. 150:129–142. http://dx.doi.org/10.1016/j.atmosres.2014.07.022.

Chen, B., Jie, D.M., Shi, M.N., Gao, P., Shen, Z.X., Uchida, M., Zhou, L.P., Liu, K.X., Hu, K., Kitagawa, H., 2015a. Characteristics of ^{14}C and ^{13}C of carbonate aerosols in dust storm events in China. Atmos. Res. 164–165. http://dx.doi.org/10.1016/j.atmosres.2015.06.003.

Chen, L., Zhang, M.G., Wang, Y.W., 2015b. Model analysis of urbanization impacts on boundary layer meteorology under hot weather conditions: a case study of Nanjing, China. Theor. Appl. Climatol. 1–16. http://dx.doi.org/10.1007/s00704-015-1535-6.

Chen, S.Y., Zhao, C., Qian, Y., Leung, L.R., Huang, J.P., Huang, Z.W., Bi, J.R., Zhang, W., Shi, J.S., Yang, L., Li, D.S., Li, J.X., 2014. Regional modeling of dust mass balance and radiative forcing over East Asia using WRF-Chem. Aeolian Res. 15:15–30. http://dx.doi.org/10.1016/j.aeolia.2014.02.001.

Chun, Y., Boo, K.O., Kim, J., Park, S.U., Lee, M., 2001. Synopsis, transport, and physical characteristics of Asian dust in Korea. J. Geophys. Res. 106:18461–18469. http://dx.doi.org/10.1029/2001JD900184.

Dentener, F.J., Carmichael, G.R., Zhang, Y., Lelieveld, J., Crutzen, P.J., 1996. Role of mineral aerosol as a reactive surface in the global troposphere. J. Geophys. Res. 101:22869–22889. http://dx.doi.org/10.1029/96JD01818.

Dong, Z.W., Li, Z.Q., Edwards, R., Wu, L.H., Zhou, P., 2011. Temporal characteristics of mineral dust particles in precipitation of Urumqi River Valley in Tian Shan, China: a comparison of alpine site and rural site. Atmos. Res. 101:294–306. http://dx.doi.org/10.1016/j.atmosres.2011.03.002.

Gao, Y., Zhang, M., Liu, Z., Wang, L., Wang, P., Xia, X., Tao, M., Zhu, L., 2015. Modeling the feedback between aerosol and meteorological variables in the atmospheric boundary layer during a severe fog-haze event over the North China Plain. Atmos. Chem. Phys. 15:4279–4295. http://dx.doi.org/10.5194/acp-15-4279-2015.

Gao, Y., Zhao, C., Liu, X.H., Zhang, M.G., Leung, R.L., 2014. WRF-Chem simulations of aerosols and anthropogenic aerosol radiative forcing in East Asia. Atmos. Environ. 92:250–266. http://dx.doi.org/10.1016/j.atmosenv.2014.04.038.

Gong, S.L., Barrie, L.A., Blanchet, J.P., 1997. Modeling sea-salt aerosols in the atmosphere: 1. Model development. J. Geophys. Res. 102:3805–3818. http://dx.doi.org/10.1029/96JD02953.

Goto, D., Nakajima, T., Dai, T., Takemura, T., Kajino, M., Matsui, H., Takami, A., Hatakeyama, S., Sugimoto, N., Shimizu, A., Ohara, T., 2015. An evaluation of simulated particulate sulfate over East Asia through global model intercomparison. J. Geophys. Res. 120:6247–6270. http://dx.doi.org/10.1002/2014JD021693.

Grell, G.A., Peckham, S.E., Schmitz, R., Mckeen, S.A., Frost, G., Skamarock, W.C., Eder, B., 2005. Fully coupled "online" chemistry within the WRF model. Atmos. Environ. 39:6957–6975. http://dx.doi.org/10.1016/j.atmosenv.2005.04.027.

Grini, A., Myhre, G., Zender, C.S., Isaksen, I.S.A., 2005. Model simulations of dust sources and transport in the global atmosphere: effects of soil erodibility and wind speed variability. J. Geophys. Res. 110, D02205. http://dx.doi.org/10.1029/2004JD005037.

Cwiertny, D.M., Young, M.A., Grassian, V.H., 2008. Chemistry and photochemistry of mineral dust aerosol. Annu. Rev. Phys. Chem. 59:27–51. http://dx.doi.org/10.1146/annurev.physchem.59.032607.093630.

Han, X., Ge, C., Tao, J.H., Zhang, M.G., Zhang, R.J., 2012. air quality modeling for a strong dust event in East Asia in March 2010. Aerosol Air Qual. Res. 12:615–628. http://dx.doi.org/10.4209/aaqr.2011.11.0191.

Han, Z.W., Li, J.W., Guo, W.D., Xiong, Z., Zhang, W., 2013. A study of dust radiative feedback on dust cycle and meteorology over East Asia by a coupled regional climate-chemistry-aerosol model. Atmos. Environ. 68:54–63. http://dx.doi.org/10.1016/j.atmosenv.2012.11.032.

He, H., Wang, Y.S., Ma, Q.X., Ma, J.Z., Chu, B.W., Ji, D.S., Tang, G.Q., Liu, C., Zhang, H.X., Hao, J.M., 2014. Mineral dust and NO_x promote the conversion of SO_2 to sulfate in heavy pollution days. Sci. Rep. 4:4172. http://dx.doi.org/10.1038/srep04172.

He, K.B., 2013. Multi-resolution Emission Inventory for China (MEIC): model framework and 1990–2010 anthropogenic emissions. International Global Atmospheric Chemistry Conference, 17–21 September, Beijing, China.

Heikes, B.G., Thompson, A.M., 1983. Effects of heterogeneous processes on NO_3, HONO and HNO_3 chemistry in the troposphere. J. Geophys. Res. 88:10883–10895. http://dx.doi.org/10.1029/JC088iC15p10883.

Holben, B.N., Eck, T.F., Slutsker, I., Tanre, D., Buis, J.P., Setzer, A., Vermote, E., Reagan, J.A., Kaufman, Y.J., Nakajima, T., Lavenu, F., Jankowiak, I., Smirnov, A., 1998. AERONET-A federated instrument network and data archive for aerosol characterization. Remote Sens. Environ. 66, 1–16.

Hong, S.Y., 2010. A new stable boundary-layer mixing scheme and its impact on the simulated East Asian summer monsoon. Q. J. R. Meteorol. Soc. 136:1481–1496. http://dx.doi.org/10.1002/qj.665.

Howell, S.G., Clarke, A.D., Shinozuka, Y., Kapustin, V., McNaughton, C.S., Huebert, B.J., 2006. Influence of relative humidity upon pollution and dust during ACE-Asia: size distributions and implications for optical properties. J. Geophys. Res. 111, D06205. http://dx.doi.org/10.1029/2004JD005759.

Huang, J.P., Minnis, P., Yi, Y.H., Tang, Q., Wang, X., Hu, Y.X., Liu, Z.Y., Ayers, K., Trepte, C., Winker, D., 2007. Summer dust aerosols detected from CALIPSO over the Tibetan Plateau. Geophys. Res. Lett. 34, L18805. http://dx.doi.org/10.1029/2007GL029938.

Hsu, S.C., Liu, S.C., Arimoto, R., Liu, T.H., Huang, Y.T., Tsai, F., Lin, F.J., Kao, S.J., 2009. Dust deposition to the East China Sea and its biogeochemical implications. J. Geophys. Res. 114, D15304. http://dx.doi.org/10.1029/2008JD011223.

Jacob, D.J., 2000. Heterogeneous chemistry and tropospheric ozone. Atmos. Environ. 34:2131–2159. http://dx.doi.org/10.1016/S1352-2310(99)00462-8.

Kang, J.Y., Tanaka, T.Y., Mikami, M., 2014. Effect of dead leaves on early spring dust emission in East Asia. Atmos. Environ. 86:35–46. http://dx.doi.org/10.1016/j.atmosenv.2013.12.007.

Kang, J.Y., Yong, S.C., Shao, Y.P., Kim, S.W., 2011. Comparison of vertical dust flux by implementing three dust emission schemes in WRF/Chem. J. Geophys. Res. 116, D09202. http://dx.doi.org/10.1016/10.1029/2010JD014649.

Koletsis, I., Giannaros, T.M., Lagouvardos, K., Kotroni, V., 2016. Observational and numerical study of the Vardaris wind regime in northern Greece. Atmos. Res. 171:107–120. http://dx.doi.org/10.1016/j.atmosres.2015.12.011.

Kumar, R., Barth, M.C., Madronich, S., Naja, M., Carmichael, G.R., Pfister, G.G., Knote, C., Brasseur, G.P., Ojha, N., Sarangi, T., 2014. Effects of dust aerosols on tropospheric chemistry during a typical pre-monsoon season dust storm in northern India. Atmos. Chem. Phys. 14:6813–6834. http://dx.doi.org/10.5194/acp-14-6813-2014.

Kutiel, H., Furman, H., 2003. Dust storms in the Middle East: sources of origin and their temporal characteristics. Indoor and Built Environ. 12:419–426. http://dx.doi.org/10.1177/1420326X03037110.

Kwun, J.H., Kim, Y.K., Seo, J.W., Jeong, J.H., You, S.H., 2009. Sensitivity of MM5 and WRF mesoscale model predictions of surface winds in a typhoon to planetary boundary layer parameterizations. Nat. Hazards 51:63–77. http://dx.doi.org/10.1007/s11069-009-9402-3.

Li, Y., An, J.L., Min, M., Zhang, W., Wang, F., Xie, P.H., 2011. Impacts of HONO sources on the air quality in Beijing, Tianjin and Hebei Province of China. Atmos. Environ. 45:4735–4744. http://dx.doi.org/10.1016/j.atmosenv.2011.04.086.

Li, J., Wang, Z., Zhuang, G., Luo, G., Sun, Y., Wang, Q., 2012. Mixing of Asian mineral dust with anthropogenic pollutants over East Asia: a model case study of a superduststorm in March 2010. Atmospheric Chemistry and Physics 12:7591–7607. http://dx.doi.org/10.5194/acp-12-7591-2012.

Liu, L.X., Huang, X., Ding, A.J., Fu, C.B., 2016. Dust-induced radiative feedbacks in north China: a dust storm episode modeling study using WRF-Chem. Atmos. Environ. 129:43–54. http://dx.doi.org/10.1016/j.atmosenv.2016.01.019.

Liu, M., Westphal, D.L., 2001. A study of the sensitivity of simulated mineral dust production to model resolution. J. Geophys. Res. 106 (D16):18099–18112. http://dx.doi.org/10.1029/2000JD900711.

Liu, M., Westphal, D.L., Wang, S.G., Shimizu, A., Sugimoto, N., Zhou, J., Chen, Y., 2003. A high-resolution numerical study of the Asian dust storms of April 2001. J. Geophys. Res. 108:8653. http://dx.doi.org/10.1029/2002JD003178.

Liu, Z., Liu, D., Huang, J., Vaughan, M., Uno, I., Sugimoto, N., Kittaka, C., Trepte, C., Wang, Z., Hostetler, C., Winker, D., 2008. Airborne dust distributions over the Tibetan Plateau and surrounding areas derived from the first year of CALIPSO lidar observations. Atmos. Chem. Phys. 8:5045–5060. http://dx.doi.org/10.5194/acp-8-5045-2008.

Lo, J.C.F., Yang, Z.L., Pielke Sr., R.A., 2008. Assessment of three dynamical climate downscaling methods using the Weather Research and Forecasting (WRF) model. J. Geophys. Res. 113, D09112. http://dx.doi.org/10.1029/2007JD009216.

Maghrabi, A.H., Al-Dosari, A.F., 2016. Effects on surface meteorological parameters and radiation levels of a heavy dust storm occurred in Central Arabian Peninsula. Atoms. Res. 182:30–35. http://dx.doi.org/10.1016/j.atmosres.2016.07.024.

Martin, R.V., Jacob, D.J., Yantosca, R.M., Chin, M., Ginoux, P., 2003. Global and regional decreases in tropospheric oxidants from photochemical effects of aerosols. J. Geophys. Res. 108:4097. http://dx.doi.org/10.1029/2002JD002622.

Michel, A.E., Usher, C.R., Grassian, V.H., 2002. Heterogeneous and catalytic uptake of ozone on mineral oxides and dusts: a Knudsen cell investigation. Geophys. Res. Lett. 29 (14). http://dx.doi.org/10.1029/2002GL014896.

Min, Q.L., Li, R., Lin, B., Joseph, E., Morris, V., Hu, Y., Li, S.W., Wang, S., 2014. Impacts of mineral dust on ice clouds in tropical deep convection systems. Atmos. Res. 143:64–72. http://dx.doi.org/10.1016/j.atmosres.2014.01.026.

Otte, T.L., 2008. The impact of nudging in the meteorological model for retrospective air quality simulations. Part I: evaluation against national observation networks. J. Appl. Meteorol. 47:1853–1867. http://dx.doi.org/10.1175/2007JAMC1790.1.

Park, R.S., Lee, S., Shin, S.K., Song, C.H., 2014. Contribution of ammonium nitrate to aerosol optical depth and direct radiative forcing by aerosols over East Asia. Atmos. Chem. Phys. 14:2185–2201. http://dx.doi.org/10.5194/acp-14-2185-2014.

Park, S.U., Chang, L.S., Lee, E.H., 2005. Direct radiative forcing due to aerosols in East Asia during a Hwangsa (Asian dust) event observed on 19–23 March 2002 in Korea. Atmos. Environ. 39:2593–2606. http://dx.doi.org/10.1016/j.atmosenv.2005.01.041.

Posfai, M., Axisa, D., Tompa, E., Freney, E., Bruintjes, R., Buseck, P.R., 2013. Interactions of mineral dust with pollution and clouds: an individual-particle TEM study of atmospheric aerosol from Saudi Arabia. Atmos. Res. 122:347–361. http://dx.doi.org/10.1016/j.atmosres.2012.12.001.

Pradhan, M., Kyriakou, G., Archibald, A.T., Papageorgiou, A.C., Kalberer, M., Lambert, R.M., 2010. Heterogeneous uptake of gaseous hydrogen peroxide by Gobi and Saharan dust aerosols: a potential missing sink for H_2O_2 in the troposphere. Atmos. Chem. Phys. 10:7127–7136. http://dx.doi.org/10.5194/acp-10-7127-2010.

Preszler Prince, A., Kleiber, P., Grassian, V.H., Young, M.A., 2007. Heterogeneous interactions of calcite aerosol with sulfur dioxide and sulfur dioxide–nitric acid mixtures. Phys. Chem. Chem. Phys. 9:3432–3439. http://dx.doi.org/10.1039/B703296J.

Santos-Alamillos, F.J., Pozo-Vazquez, D., Ruiz-Arias, J.A., Tovar-Pescador, J., 2015. Influence of land-use misrepresentation on the accuracy of WRF wind estimates: evaluation of GLCC and CORINE land-use maps in southern Spain. Atmos. Res. 157:17–28. http://dx.doi.org/10.1016/j.atmosres.2015.01.006.

Shao, Y.P., 2004. Simplification of a dust emission scheme and comparison with data. J. Geophys. Res. 109, D10202. http://dx.doi.org/10.1029/2003JD004372.

Shao, Y.P., Lu, H., 2000. A simple expression for wind erosion threshold friction velocity. J. Geophys. Res. 105:22437–22443. http://dx.doi.org/10.1029/2000JD900304.

Shimizu, A., Sugimoto, N., Matsui, I., Arao, K., Uno, I., Murayama, T., Kagawa, N., Aoki, K., Uchiyama, A., Yamazaki, A., 2004. Continuous observations of Asian dust and other aerosols by polarization lidars in China and Japan during ACE-Asia. J. Geophys. Res. 109:D19S17. http://dx.doi.org/10.1029/2002JD003253.

Skamarock, W.C., Klemp, J.B., Dudhia, J., Gill, D.O., Barker, D.M., Duda, M.G., Huang, X.Y., Wang, W., Powers, J.G., 2008. A Description of the Advanced Research WRF Version 3. National Center for Atmospheric Research Technical Note:p. 113 NCAR/TN-475 + STR. 10.5065/D68S4MVH.

Sokolik, I.N., Toon, O.B., 1996. Direct radiative forcing by anthropogenic airborne mineral aerosols. Nature 381:681–683. http://dx.doi.org/10.1038/381681a0.

Su, L., Fung, J.C.H., 2015. Sensitivities of WRF-Chem to dust emission schemes and land surface properties in simulating dust cycles during springtime over East Asia. J. Geophys. Res. 120:11215–11230. http://dx.doi.org/10.1002/2015JD023446.

Sugimoto, N., Shimizu, A., Matsui, I., Uno, I., Arao, K., Dong, X.H., Zhao, S.L., Zhou, J., Lee, C.H., 2005. Study of Asian dust phenomena in 2001–2003 using a network of continuously operated polarization lidars. Water Air Soil Pollut. 5:145–157. http://dx.doi.org/10.1007/s11267-005-0732-1.

Tegen, I., Schepanski, K., 2009. The global distribution of mineral dust. IOP Conf. Ser.: Earth Environ. Sci. 7:012001. http://dx.doi.org/10.1088/1755-1307/7/1/012001.

Wang, K., Zhang, Y., Nenes, A., Fountoukis, C., 2012. Implementation of dust emission and chemistry into the Community Multiscale Air Quality modeling system and initial application to an Asian dust storm episode. Atmospheric Chemistry and Physics 12: 10209–10237. http://dx.doi.org/10.5194/acp-12-10209-2012.

Wang, R.X., Liu, B., Li, H.R., Zou, X.Y., Wang, J.P., Liu, W., Cheng, H., Kang, L.Q., Zhang, C.L., 2016. Variation of strong dust storm events in Northern China during 1978–2007. Atmos. Res. 183:166–172. http://dx.doi.org/10.1016/j.atmosres.2016.09.002.

Wang, Y., Zhang, Q.Q., He, K., Zhang, Q., Chai, L., 2013. Sulfate-nitrate-ammonium aerosols over China: response to 2000–2015 emission changes of sulfur dioxide, nitrogen oxides, and ammonia. Atmos. Chem. Phys. 13:2635–2652. http://dx.doi.org/10.5194/acp-13-2635-2013.

White, B.R., 1979. Soil transport by winds on Mars. J. Geophys. Res. 84:4643–4651. http://dx.doi.org/10.1029/JB084iB09p04643.

Willmott, C.J., 1981. On the validation of models. Phys. Geogr. 2:184–194. http://www.tandfonline.com/doi/citedby/10.1080/02723646.1981.10642213.

Wu, C.L., Lin, Z.H., 2013. Uncertainty in dust budget over East Asia simulated by WRF/Chem with six different dust emission schemes. Atmos. Ocean. Sci. Lett. 6:428–433. http://dx.doi.org/10.3878/j.issn.1674-2834.13.0045.

Wu, L., Su, H., Jiang, J.H., Read, W.G., 2012. Hydration or dehydration: competing effects of upper tropospheric cloud radiation on the TTL water vapor. Atmos. Chem. Phys. 12: 7727–7735. http://dx.doi.org/10.5194/acp-12-7727-2012.

Yasunari, T.J., Colarco, P.R., Lau, W.K.M., Osada, K., Kido, M., Mahanama, S.P.P., Kim, K., Silva, A.M., 2016. Total dust deposition flux during precipitation in Toyama, Japan, in the spring of 2009: a sensitivity analysis with the NASA GEOS-5 Model. Atmos. Res. 167:298–313. http://dx.doi.org/10.1016/j.atmosres.2015.08.005.

Ying, Z.M., Tie, X.X., Madronich, S., Li, G.H., Massie, S., 2011. Simulation of regional dust and its effect on photochemistry in the Mexico City area during MILAGRO experiment. Atmos. Environ. 45:2549–2558. http://dx.doi.org/10.1016/j.atmosenv.2011.02.018.

Yu, X.N., Zhu, B., Yin, Y., Yang, J., Li, Y.W., Bu, X.L., 2011. A comparative analysis of aerosol properties in dust and haze-fog days in a Chinese urban region. Atmos. Res. 99 (2): 241–247. http://dx.doi.org/10.1016/j.atmosres.2010.10.015.

Zaveri, R.A., Easter, R.C., Fast, J.D., Peters, L.K., 2008. Model for simulating aerosol interactions and chemistry (MOSAIC). J. Geophys. Res. 113, D13204. http://dx.doi.org/10.1029/2007JD008782.

Zaveri, R.A., Peters, L.K., 1999. A new lumped structure photochemical mechanism for large-scale applications. J. Geophys. Res. 104:30387–30415. http://dx.doi.org/10.1029/1999JD900876.

Zender, C.S., Miller, R., Tegen, I., 2004. Quantifying mineral dust mass budgets: terminology, constraints, and current estimates. Eos Trans. AGU 85:509–512. http://dx.doi.org/10.1029/2004EO480002.

Zhang, D.F., Zakey, A.S., Gao, X.J., Giorgi, F., Solmon, F., 2009. Simulation of dust aerosol and its regional feedbacks over East Asia using a regional climate model. Atmos. Chem. Phys. 9:1095–1110. http://dx.doi.org/10.5194/acp-9-1095-2009.

Zhang, Y.L., Kang, S.C., Zhang, Q.G., Grigholm, B., Kaspari, S., You, Q.L., Qin, D.H., Mayewski, P.A., Cong, Z.Y., Huang, J., Sillanpaa, M., Chen, F., 2015. A 500 year atmospheric dust deposition retrieved from a Mt. Geladaindong ice core in the central Tibetan Plateau. Atmos. Res. 166:1–9. http://dx.doi.org/10.1016/j.atmosres.2015.06.007.

Zhang, X.Y., Arimoto, R., An, Z.S., 1997. Dust emission from Chinese desert sources linked to variations in atmospheric circulation. J. Geophys. Res. 102:28041–28047. http://dx.doi.org/10.1029/97JD02300.

Zhao, C., Liu, X., Leung, L.R., Hagos, S., 2011. Radiative impact of mineral dust on monsoon precipitation variability over West Africa. Atmos. Chem. Phys. 11:1879–1893. http://dx.doi.org/10.5194/acp-11-1879-2011.

Zhao, C., Liu, X., Leung, L.R., Johnson, B., McFarlane, S.A., Gustafson Jr., W.I., Fast, J.D., Easter, R., 2010. The spatial distribution of mineral dust and its shortwave radiative forcing over North Africa: modeling sensitivities to dust emissions and aerosol size treatments. Atmos. Chem. Phys. 10:8821–8838. http://dx.doi.org/10.5194/acp-10-8821-2010.

Zhao, T.L., Gong, S.L., Zhang, X.Y., McKendry, I.G., 2003. Modeled size-segregated wet and dry deposition budgets of soil dust aerosol during ACE-Asia 2001: implications for trans-Pacific transport. J. Geophys. Res. 108 (D23):8665. http://dx.doi.org/10.1029/2002JD003363.

Zheng, B., Zhang, Q., Zhang, Y., He, K.B., Wang, K., Zheng, G.J., Duan, F.K., Ma, Y.L., Kimoto, T., 2015. Heterogeneous chemistry: a mechanism missing in current models to explain secondary inorganic aerosol formation during the January 2013 haze episode in North China. Atmos. Chem. Phys. 15:2031–2049. http://dx.doi.org/10.5194/acp-15-2031-2015.

Zhu, S., Butler, T., Sander, R., Ma, J., Lawrence, M.G., 2010. Impact of dust on tropospheric chemistry over polluted regions: a case study of the Beijing megacity. Atmos. Chem. Phys. 10:3855–3873. http://dx.doi.org/10.5194/acp-10-3855-2010.